TECHNISCHE UNIVERSITÄT WIEN

DIPLOMARBEIT

Electrochemical behaviour of $La_{0.6}Sr_{0.4}CoO_{3-\delta}$ thin film microelectrodes upon anodic polarisation

zur Erlangung des akademischen Grades

Diplom-Ingenieur

im Rahmen des Studiums

Physikalische Energie- und Messtechnik

eingereicht von

Martin Krammer
Matrikelnummer 01129566

ausgeführt am Institut für Chemische Technologien und Analytik
der Fakultät für Technische Chemie der Technischen Universität Wien

Betreuung
Betreuer: Univ.Prof. Dipl.-Phys. Dr.rer.nat. Jürgen Fleig
Mitwirkung: Univ.Ass. Dipl.-Ing. Alexander Schmid, BSc

Wien, 12.12.2019

(Martin Krammer) (Jürgen Fleig)

Abstract

Solid oxide electrolysis cells (SOECs) have received growing attention in the last few years as they offer a way to highly efficient production of hydrogen. The high operating temperatures (700–900 °C) of SOECs are favourable because of a lower electrical energy demand and improved reaction kinetics compared to low temperature electrolysis. However, this technology still faces various problems concerning the stability and durability of the stack and cell components. In many cases the air electrode is the limiting component due to degradation effects. Therefore, efforts are being made to characterise and optimise the performance of the oxygen electrode. The perovskite-type oxide $La_{0.6}Sr_{0.4}CoO_{3-\delta}$ (LSC) is a promising material for the air electrode due to its mixed ionic-electronic conductivity and high catalytic activity for the oxygen exchange reaction. Although LSC has been extensively tested as air electrode in solid oxide fuel cells (SOFCs), comparatively few studies have been made on LSC in the SOEC mode.

In this work, the behaviour of LSC thin film microelectrodes at varying anodic DC voltages was investigated via electrochemical impedance spectroscopy. Oxygen exchange kinetics and defect chemistry were analysed by extracting the corresponding fit parameters.

A permanent degradation of the oxygen exchange resistance over time was observed. Nevertheless, strong short-term performance improvements were obtained by applying high anodic DC voltages. The defect chemistry of the electrodes was investigated by analysing the chemical capacitance at different anodic voltages. After heating the samples for several hours at around 600 °C or after applying high bias up to 1 V an unexpected peak of the chemical capacitance was obtained at overpotentials higher than 100 mV. Correlations of these capacitive effects with variations of the oxygen exchange kinetics were also investigated. Supposedly, strontium segregation to the surface and a consequential formation of A-site vacancies in the bulk of the electrodes is responsible for this peak. Hence, a novel defect chemical mechanism is suggested to contribute to the chemical capacitance of oxides.

Kurzfassung

Festoxidelektrolysezellen (SOECs) wurde in den letzten Jahren zunehmend Aufmerksamkeit geschenkt, da sie eine hocheffiziente Produktion von Wasserstoff ermöglichen. Die hohen Betriebstemperaturen (700–900 °C) von Festoxidelektrolysezellen sind vorteilhaft aufgrund eines geringeren elektrischen Energiebedarfs und verbesserter Reaktionskinetik im Vergleich zur Niedertemperaturelektrolyse. Allerdings steht diese Technologie noch vor einigen Problemen im Bereich der Stabilität und Beständigkeit der Stack- und Zellkomponenten. Die Luftelektrode ist aufgrund von Degradationseffekten oft die limitierende Komponente. Daher werden viele Anstrengungen unternommen, um die Leistung der Luftelektrode zu untersuchen und zu optimieren. Das perowskitische Oxid $La_{0.6}Sr_{0.4}CoO_{3-\delta}$ (LSC) ist aufgrund seiner gemischt elektronisch-ionischen Leitfähigkeit und der hohen katalytischen Aktivität für die Sauerstoffaustauschreaktion ein vielverprechendes Material für die Luftelektrode. Obowhl LSC als Luftelektrode für Festoxidbrennstoffzellen (SOFCs) schon ausführlich getestet wurde, gibt es vergleichsweise wenig Studien über LSC im SOEC-Modus.

Im Rahmen dieser Arbeit wurde das Verhalten von LSC Dünnfilm-Mikroelektroden bei unterschiedlichen anodischen Gleichspannungen mit Hilfe von elektrochemischer Impedanzspektroskopie untersucht. Die Sauerstoffaustauschkinetik und die Defektchemie der Elektroden wurden mit Hilfe der entsprechenden Fit-Parameter analysiert.

Es wurde eine dauerhafte Zunahme des Sauerstoffaustausch-Widerstandes im Laufe der Zeit festgestellt. Dennoch konnten kurzfristig starke Leistungsverbesserungen durch Anlegen von hohen anodischen Gleichspannungen beobachtet werden. Die Defektchemie der Elektroden wurde mittels Analyse der chemischen Kapazität bei verschiedenen anodischen Spannungen untersucht. Nach mehrstündigem Heizen der Proben auf etwa 600 °C oder nach Anlegen einer hohen Spannung bis zu 1 V wurde ein unerwarteter Anstieg der chemischen Kapazität bei Überspannungen von über 100 mV beobachtet. Korrelationen dieser kapazitiven Effekte mit Änderungen in der Sauerstoffaustauschkinetik wurden untersucht. Es wird vermutet, dass Segregation von Strontium an die Oberfläche und eine daraus resultierende Bildung von A-Platz-Leerstellen im Volumen der Elektroden für diesen Anstieg verantwortlich sind. Entsprechend konnte ein neuer defektchemischer Mechanismus vorgeschlagen werden, der zur chemischen Kapazität von Oxiden beiträgt.

Contents

1 Introduction

The global ever-growing demand for energy leads to various challenges concerning economic, social and ecological issues. In order to meet the growing demand, fossil fuels play the key role as they account for over 80 % of the world energy production [1]. Given the climate goals of the Paris agreement, the energy sector faces drastic changes as it accounts for two thirds of total greenhouse gas emissions [2]. Therefore, great efforts are being made to increase the share of renewable energy production. However, renewable energy production often suffers from difficulties concerning supply and demand matching. Thus, energy storage is the key to solve these problems and hydrogen is a suitable energy carrier for this issue. Excess electrical energy can be converted to hydrogen with the help of electrolysis in times when the demand is low. Fuel cells can be used to transform the stored hydrogen back to electricity when it is needed. Furthermore, hydrogen could be used as a fuel in the mobility sector and is considered as a replacement for fossil fuels in industrial processes such as steel production. Hence, a hydrogen economy would enable a coupling of the electricity, the industrial, the mobility and the heating sectors. At the moment, hydrogen use is dominated by industrial applications. The major single uses of hydrogen are oil refining (33 %), ammonia production (27 %) and methanol production (11 %). Today's hydrogen production relies on fossil resources with 76 % produced from natural gas and almost all the rest from coal. As a consequence, global yearly hydrogen production is responsible for 820 Mt CO_2 - corresponding to the combined annual CO_2 emissions of Indonesia and the United Kingdom. In contrast, electrolysis accounts only for 2 % of global hydrogen production [3].
A higher share of water electrolysis combined with renewable electricity production would not only avoid emissions when replacing current major hydrogen production technologies, but also allows zero-carbon developments in other sectors as described above. The principle of water electrolysis is to split water into hydrogen and oxygen by supplying electrical (and thermal) energy. That is the reverse reaction which occurs in a fuel cell. The different water electrolysis technologies can be classified according to their different electrolytes, that separate the two half reactions at the cathode (hydrogen evolution) and at the anode (oxygen evolution). The main technologies are alkaline electrolysis (AEL), polymer electrolyte membrane electrolysis (PEMEL) and solid oxide electrolysis (SOEL) [4] [5]. AEL and PEMEL operate at comparatively low temperatures (60–90 °C) while SOEL works at high temperatures (700–900 °C)[4]. These high operating temperatures in solid oxide

electrolysis cells (SOECs) are favourable because of a lower electrical energy demand and improved reaction kinetics compared to low temperature electrolysis [6]. What is more, SOECs can also utilise high temperature waste heat and excess energy from power plants during off-peak hours to further optimise their efficiency [5]. Consequently, SOECs have attracted great interest in recent years, as they offer high efficiencies and considerable power.
In a solid oxide electrolysis cell (SOEC) water steam is fed to the hydrogen electrode (cathode) where it is reduced to hydrogen:

$$2\,H_2O + 4\,e^- \longrightarrow 2\,H_2 + 2\,O^{2-} \tag{1.1}$$

The generated oxygen ions get incorporated at the cathode and pass through the ion conducting electrolyte to the anode. At the anode, oxygen is produced and electrons are released:

$$2\,O^{2-} \longrightarrow O_2 + 4\,e^- \tag{1.2}$$

The resulting overall reaction is:

$$2\,H_2O \longrightarrow 2\,H_2 + O_2 \tag{1.3}$$

In addition, SOECs can be used to produce syngas (H_2 and CO) by coelectrolysis of water steam and carbon dioxide:

$$H_2O + CO_2 \longrightarrow H_2 + CO + O_2 \tag{1.4}$$

Thus, with the use of CO_2 capture from fossil fuels, SOECs offer a low-carbon production for syngas. The working principle and typical setup of an SOEC for hydrogen production is shown in Figure 1.1. Typically, the materials used in an SOEC are similar to those used in a solid oxide fuel cell (SOFC). Although the structure and the materials of SOECs and SOFCs are almost identical, different degradation phenomena are observed in the SOEC mode due to inverse operating conditions. Despite recent efforts, further investigations are required to understand degradation mechanisms of various materials in the SOEC mode. A cermet based on nickel and a ceramic such as Y_2O_3-stabilised ZrO_2 (YSZ) is the most common material for the cathode of an SOEC [7]. Although nickel is widely used, there are several reports on the degradation of this material under electrolysis mode [8] [9] [10]. Moreover, small amounts of hydrogen at the cathode are required in order to avoid re-oxidation of Ni to NiO [11]. It was shown that the incorporation of electrocatalytically active nanoparticles such as gadolinium-doped ceria (GDC), $Sm_{0.2}Ce_{0.8}O_{1.9}$ (SDC), and $Mo_{0.1}Ce_{0.9}O_2$ oxides in a Ni-YSZ cermet hydrogen electrode enhances the ionic conductivity and improves the triple phase boundary length resulting in a higher electrocatalytic

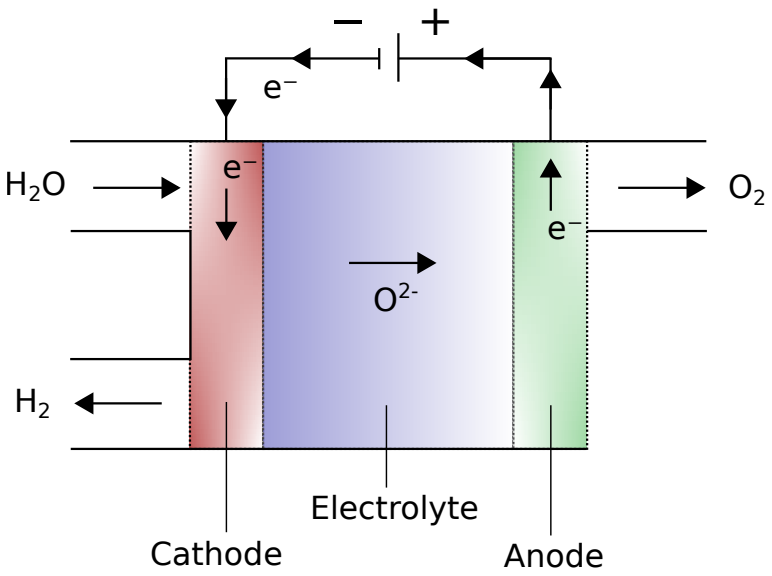

Figure 1.1: Working principle and setup of a SOEC

activity and/or operating stability for the water-splitting reaction [12] [13] [14]. Oxide materials like $(La_{0.75}Sr_{0.25})_{0.95}Cr_{0.5}Mn_{0.5}O_3$ (LSCM) [15], (La,Sr)TiO_3 [16], Sr_2FeNbO_6 [17] and $Sr_{0.94}Ti_{0.9}Nb_{0.1}O_{3-\delta}$ [18] are also investigated as cathode materials. Additionally, it was observed that Fe and Ni nanoparticles increase the electrocatalytic activity as well as the current efficiency of SOEC cathodes [19] [20].
The most common electrolyte is Y_2O_3-stabilised ZrO_2 (YSZ) because it offers the best combination of ionic conductivity and stability [21] at the high operating temperatures of SOECs. Ceria containing materials have been also proposed as electrolytes for SOECs but they suffer from degradation due to the reduction of Ce^{4+} to Ce^{3+} [22] [23]. It was found that $La_{0.9}Sr_{0.1}Ga_{0.8}Mg_{0.2}O_3$ (LSGM) has a higher ionic conductivity than YSZ. However, the main problem with LSGM is that it reacts with the Ni electrode to form lanthanum nickelates. A thin interlayer of $Ce_{0.8}Sm_{0.2}O_{1.9}$ at the electrode-electrolyte interface would prevent this reaction, but ceria leads to degradation effects as mentioned above [21].
Since the oxygen electrode is often the limiting component, efforts are being made to optimise its performance. Strontium-doped lanthanum manganite (LSM) has been extensively used as oxygen electrode for SOECs because of its high electronic conductivity, reasonable catalytic properties at elevated temperatures and excellent thermal compatibility with the YSZ electrolyte [24]. Nevertheless, LSM has poor ionic conductivity and the oxygen oxidation reaction occurs mainly at the triple phase boundary [25]. Furthermore, several authors have reported on the accelerated degradation as a consequence of delamination of LSM when used as the oxygen electrode in SOECs [26] [27] [28] [29]. Therefore, alternative

oxygen electrode materials are proposed and investigated. Mixed ionic-electronic conducting (MIEC) perovskite type oxides such as lanthanum strontium ferrite (LSF), lanthanum strontium cobalt ferrite (LSCF), strontium copper ferrite (LSCuF) and lanthanum strontium cobaltite (LSC) seem to be promising candidates because of their good performance in the SOFC mode [30] [31] [32] [33].
Although these materials have been thoroughly investigated in the SOFC mode, comparatively few studies have been made for the use in SOECs. Hence, in order to gain a better understanding of the electrode performances and to find ways to improve their stability, more research in the area of SOECs is necessary.
The aim of this study was to investigate the behaviour of LSC thin film microelectrodes upon anodic polarisation which corresponds to the SOEC mode. Electrochemical impedance spectroscopy was used to characterise the LSC microelectrodes. Impedance measurements were evaluated by fitting the obtained spectra with suitable equivalent circuits. Oxygen exchange kinetics and defect chemistry upon different anodic polarisations were evaluated. In order to investigate the reversibility of the observed effects, bias voltage cycles were applied. A permanent degradation of the electrode oxygen exchange kinetics has been revealed. However, a strong activation occurred upon high anodic polarisations. Moreover, the defect chemistry - investigated by means of chemical capacitance - of pristine electrodes showed a different behaviour than that of already degraded electrodes. Therefore, a link between the chemical capacitance upon anodic polarisation and the level of degradation is suggested.

2 Theoretical background

2.1 Lanthanum strontium cobaltite

2.1.1 Crystal structure

$La_{1-x}Sr_xCoO_{3-\delta}$ crystallises in the perovskite-type structure with the chemical composition ABO_3. The A site is occupied by the larger cation, whereas the smaller cation is placed at the B site. The A site cation is coordinated by 12 oxygen ions and the B site cation is surrounded by an octahedron of oxygen ions resulting in a 6-fold coordination. In LSC A corresponds either to La^{3+} or to Sr^{2+} and B corresponds to Co^{3+}. The idealised cubic perovskite structure of LSC is shown in Figure 2.1.

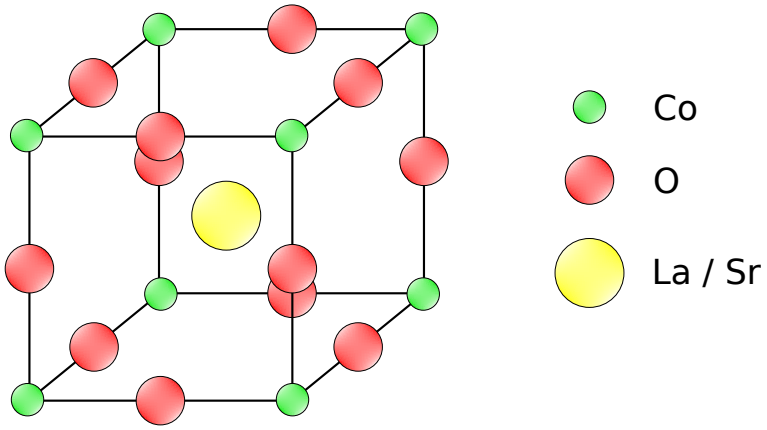

Figure 2.1: A-centered view of the ideal cubic perovskite structure of LSC

The ionic radii in perovskite materials with the composition ABO_3 are in a specific relationship to each other, which is determined by the Goldschmidt tolerance factor [34]:

$$t = \frac{(r_A + r_O)}{\sqrt{2} \cdot (r_B + r_O)} \tag{2.1}$$

For the ideal cubic perovskite structure the value of the Goldschmidt tolerance factor is 1.

In general, stable perovskites are predicted to have a tolerance factor between 0.8 and 1.1. For the calculation of the tolerance factor of $La_{0.6}Sr_{0.4}CoO_{3-\delta}$, which is the configuration that was used in this work, ion radii shown in Table 2.1 were taken from the work done by R. D. Shannon [35].

Table 2.1: Radii of ions taken from measurements of R. D. Shannon [35]

Ion species	Ion radii $r_i\,(nm)$
Sr^{2+}	0.144
La^{3+}	0.136
Co^{3+}	0.058
O^{2-}	0.135

The actual crystal structure of LSC depends on the Sr dopant concentration and on the temperature. The different coordination numbers had to be considered for the ion radii and the radius of Co^{3+} was determined by calculating the mean of the high-spin and the low-spin form of Co^{3+} corresponding to a 50:50 mixture of the two forms at room temperature [36]. A tolerance factor of 1.005 was calculated for $La_{0.6}Sr_{0.4}CoO_{3-\delta}$ with the effective ionic radius of the A-site cation:

$$r_{A,eff} = 0.4 \cdot r_{Sr^{2+}} + 0.6 \cdot r_{La^{3+}} \tag{2.2}$$

Powder XRD studies of $La_{1-x}Sr_xCoO_{3-\delta}$ at room temperature by R.H.E. van Doorn et al. revealed a rhombohedrically distorted perovskite structure for $x \leq 0.5$, whereas a cubic perovskite lattice was observed for $x > 0.5$ [37]. In addition, Mastin et al. showed that the rhombohedral distortion of $La_{1-x}Sr_xCoO_{3-\delta}$ ($0 \leq x \leq 0.5$) from cubic symmetry decreases nearly linearly with increasing temperature up to the phase transition to the cubic perovskite structure. This phase transition temperature was found to decrease rapidly with increasing Sr dopant concentration. For $La_{0.6}Sr_{0.4}CoO_{3-\delta}$ the phase transition temperature was determined to be 450 °C [38]. Therefore, under the applied measurement conditions in this work and under the usual SOEC operating conditions, LSC, in the used configuration, exists in the cubic perovskite structure.

2.1.2 Defect chemistry

In order to understand chemical and electrical properties of solids and to be able to tailor these, it is necessary to study defects, which are the deviations from the ideal crystal structure. In solid state ionics these properties are often determined by zero-dimensional defects, which are also referred to as point defects. A vacancy, which occurs if an atom is absent from its nominally occupied position, is such a point defect. Another example for a point defect is called an interstitial atom, which arises if an extra atom gets incorporated into the crystal structure at a nominally unoccupied site. Other examples would be excess electrons and electron holes. A suitable notation for point defects was introduced by Kröger and Vink [39]:

$$S_C^L \tag{2.3}$$

This notation refers to the deviation from the perfect crystal structure which is caused by the point defect. Here, S stands for the species which may be an atom, ion, electron (e), electron hole (h) or a vacancy (V). The subscript L describes the location of the species, which can be a lattice site of an atom or an interstitial site (i) that is nominally not occupied in the perfect crystal. The superscript C characterises the charge relative to that in the perfect crystal. A point ($\cdot$) stands for positive charge, whereas an apostrophe ($'$) indicates a negative charge. Furthermore, an x as superscript represents relative charge neutrality.
It is obvious that the Kröger-Vink notation is very useful to describe the effects of Sr doping in $LaCoO_3$. In LSC, Sr^{2+} gets incorporated on the La^{3+} site because of their similar ionic radii. Hence, a reaction has to take place in order to restore charge neutrality. In general, cobalt ions assume valence states between 2+ and 4+, while La^{3+}, Sr^{2+} and O^{2-} have fixed valence states. That is why cobalt ions are largely responsible for the restoration of charge neutrality. Results of Jonker and Van Santen [40] showed that the concentration of Co^{4+} in $La_{1-x}Sr_xCoO_{3-\delta}$ is close to the Sr content x for $x < 0.3$, suggesting electronic charge compensation by oxidation of Co and preserving the oxygen content close to stoichiometry. However, according to their data the concentration of Co^{4+} saturates for $0.3 < x < 0.7$ and decreases for $x > 0.7$. This indicates that $La_{1-x}Sr_xCoO_{3-\delta}$ shows oxygen deficiency for $x > 0.3$. Furthermore, Mizusaki et al. [41] revealed that oxygen deficiency δ in LSC increases with increasing temperature, increasing Sr content and decreasing oxygen partial pressure. They observed that at a temperature of 800 °C and for a Sr content of $x \leq 0.2$, the increase in x results mainly in an increase of the mean Co valence, whereas for $0.2 < x < 0.5$ the increase in x mainly leads to an increase in δ. For $x > 0.5$, the mean cobalt valence is again increasing with increasing x.

These results show that at certain conditions, the main consequence of Sr doping is the formation of oxygen vacancies $V_O^{\bullet\bullet}$ due to the following defect reactions:

$$SrO \longrightarrow Sr'_{La} + h^{\bullet} + O_O^{\times} \tag{2.4a}$$

$$2\,Co_{Co}^{\times} \rightleftharpoons e'(Co'_{Co}) + h^{\bullet}(Co^{\bullet}_{Co}) \tag{2.4b}$$

$$O_O^{\times} + 2\,h^{\bullet}(Co^{\bullet}_{Co}) \rightleftharpoons \frac{1}{2}\,O_O^{\times} + V_O^{\bullet\bullet} + 2\,Co_{Co}^{\times} \tag{2.4c}$$

The Sr doping, which is described by equation 2.4a, is thought to proceed completely, while the charge disproportionation (equation 2.4b) and the oxygen exchange reaction (equation 2.4c) are in equilibrium with the prevailing atmosphere at a certain temperature [42]. The existence of oxygen vacancies is responsible for the ionic conductivity of LSC.
It was shown that a Sr content of $x \leq 0.2$ in $La_{1-x}Sr_xCoO_3$ leads to a metallic behaviour due to the formation of Co 3d states above the Fermi level [43]. Thus, the charge disproportionation model, described by equation 2.4b, has to be reviewed critically as it assumes localised non-interacting point defects. For that reason, Lankhorst and Bouwmester [44] proposed the itinerant electron model. In this model the oxygen nonstoichiometry is derived from the assumption that the conduction electrons occupy states of a partially filled electron band. In this case, the oxidation reaction is described by the following equilibrium:

$$O_2^{gas} + 2\,V_O^{\bullet\bullet} + 4\,e' \rightleftharpoons 2\,O_O^{\times} \tag{2.5}$$

This model assumes that oxygen vacancies are noninteracting and randomly distributed among oxygen sites. The corresponding chemical potential for the incorporation of oxygen into the perovskite lattice is given by equation 2.6.

$$\mu_{O_2^{gas}} = H_{O_2} - TS_{O_2} + RT \cdot ln\left(\frac{[O_O^{\times}]^2}{[V_O^{\bullet\bullet}]^2[e']^4}\right) \tag{2.6}$$

H_{O_2} and S_{O_2} are the respective energy and entropy associated with placing one oxygen molecule from vacuum into the oxide lattice by filling up two oxygen vacancies. Lankhorst and Bouwmester related the chemical potential of electrons $\mu_{e'}$ to the electron occupancy defined as follows:

$$[e'] = \frac{N_{e'}}{N} \tag{2.7}$$

Here, $N_{e'}$ stands for the total number of conduction electrons in the partially filled electron

band with N sites. In such bands the chemical potential of electrons is equal to the Fermi energy ϵ_F. The electron occupancy $[e']$ can be obtained by integrating the Fermi-Dirac distribution function $f(\epsilon)$ multiplied by the density of states $g(\epsilon)$ over the total bandwidth:

$$[e'] = \int_{\epsilon_b}^{\epsilon_t} g(\epsilon) f(\epsilon) d\epsilon \approx \int_{\epsilon_b}^{\epsilon_F} g(\epsilon) d\epsilon \tag{2.8}$$

ϵ_b and ϵ_t stand for the energies at the bottom and the top of the band, respectively. The approximation in equation 2.8 is based on the assumption that all electron states below ϵ_F are occupied, whereas those above ϵ_F are unoccupied. Furthermore, it is assumed that the bandwidth is large compared to $k_B T$ and therefore the site limitation of the Fermi-Dirac distribution can be neglected. The chemical potential of electrons $\mu_{e'}$ can be derived by using the first-order Tailor expansion of equation 2.8:

$$[e'] = [e']^0 + \frac{\delta[e']}{\delta\epsilon} \cdot \Delta\epsilon \tag{2.9a}$$

$$\Delta\epsilon = \frac{[e'] - [e']^0}{g(\epsilon_F)} \tag{2.9b}$$

$$\mu_{e'} = \epsilon_F([e']) = \epsilon_F([e']^0) + \frac{[e'] - [e']^0}{g(\epsilon_F)} = \epsilon_F([e']^0) + \Delta\epsilon \tag{2.9c}$$

$[e']^0$ is defined as the electron occupation number when there are no vacancies. Consequently, the Fermi level moves upwards as electrons are donated to the band, at a rate determined by the invariant density of states at the Fermi level. This formalism is commonly referred as electron gas rigid band model [45]. From combining equation 2.6 and 2.9c with the charge neutrality condition [46]

$$[e'] - [e']^0 = 2[V_O^{\bullet\bullet}] - [Sr'_{La}] \tag{2.10a}$$

and

$$\mu_{e'} = \epsilon_F([e']^0) + RT \cdot ln([e']^0) \tag{2.10b}$$

the chemical potential of oxygen can be calculated as:

$$\mu_{O_2^{gas}} = H_{O_2} - TS_{O_2} - \frac{4 \cdot (2[V_O^{\bullet\bullet}] - [Sr'_{La}])}{g(\epsilon_F)} + 2RTln\left(\frac{[O_O^{\times}]}{[V_O^{\bullet\bullet}]}\right) \tag{2.10c}$$

Lankhorst et al. showed that the electron gas rigid band model predicts the relationship of oxygen nonstoichiometry, temperature and oxygen partial pressure quite well by comparing experimental data from coulometric titration to fits based on equation 2.10c [44] [47]. However, they also observed that the partial energy and entropy of oxygen show significant variations with respect to oxygen nonstoichiometry and temperature, which cannot be explained within the itinerant electron model. These variations may be due to a partial ordering of oxygen vacancies at high oxygen nonstoichiometry and low temperature. Nevertheless, at low oxygen nonstoichiometry, the assumption of randomly distributed oxygen vacancies remains valid [47].

2.2 Chemical capacitance

LSC as a mixed ionic-electronic conducting perovskite has two different charge carriers. These are oxygen vacancies for the ionic conductivity and electrons or electron holes for the electronic conductivity. As described in subsection 2.1.2, the chemical potential of oxygen determines the equilibrium concentrations of these charge carriers and therefore also the stoichiometry of the material. What is more, the oxygen chemical potential itself depends on the Sr dopant concentration, the oxygen partial pressure and the applied voltage. By changing these parameters the equilibrium is shifted, which can be interpreted as transfer of charge between ionic and electronic charge carriers. This transfer causes a capacitive response to an applied voltage, which is referred to as chemical capacitance [48]. This chemical capacitance can be interpreted as a measure of readiness for stoichiometry changes and describes the electroneutral chemical storage of charge, unlike an electrostatic capacitor with charge separation [49]. Therefore, the chemical capacitance of a material contains important information about its defect chemistry.
The chemical capacitance of an oxide is defined as follows [50]:

$$C_{chem} = 4F^2 V n^0 \cdot \left(\frac{\partial \mu_O}{\partial c_O}\right)^{-1} \tag{2.11}$$

In equation 2.11 F stands for the Faraday constant and V for the sample's volume. The determining factor of equation 2.11 is the derivative of the oxygen chemical potential μ_O with respect to the normalised oxygen concentration c_O. The oxygen concentration is normalised with respect to the absolute concentration of oxygen sites n^0. Thus, c_O is directly related to the nonstoichiometry of the material [49]. The chemical potential of oxygen is determined by the chemical potential of oxide ions and electrons:

$$\mu_O = \mu_{O^{2-}} - 2\mu_{e^-} \tag{2.12}$$

Moreover, the oxygen chemical potential can be written as:

$$\mu_O = -\mu_V + 2z_{eon}\mu_{eon} \tag{2.13}$$

eon stands either for electrons (e) or holes (h) and z_{eon} is the corresponding charge number. The changes in concentration of oxygen and oxygen vacancies must balance each other, which is expressed by:

$$dc_O = -dc_V \tag{2.14}$$

Local charge neutrality is described by:

$$dc_{eon} = -2z_{eon}dc_V = 2z_{eon}dc_O \tag{2.15}$$

By differentiating equation 2.13 with respect to c_O and combining with equations 2.14 and 2.15, the following expression is obtained:

$$\frac{\partial\mu_O}{\partial c_O} = -\frac{\partial\mu_V}{\partial c_O} + 2z_{eon}\frac{\partial\mu_{eon}}{\partial c_O} = \frac{\partial\mu_V}{\partial c_V} + 4\frac{\partial\mu_{eon}}{\partial c_{eon}} \tag{2.16}$$

The chemical potential of defects consists of the chemical potential under standard conditions μ_d^0 and of a term regarding concentration changes. If it is assumed that the defects d are diluted, the chemical potential can be expressed as follows:

$$\mu_d = \mu_d^0 + RT \cdot ln(c_d) \tag{2.17}$$

c_d is the defect concentration n_d, normalised to n^0:

$$c_d = \frac{n_d}{n^0} \tag{2.18}$$

Finally, an expression for C_{chem} of oxides is obtained reflecting its dependence on defect concentrations:

$$C_{chem} = \frac{4F^2Vn^0}{RT}\left(\frac{1}{c_V} + \frac{4}{c_{eon}}\right)^{-1} = \frac{F^2V}{RT}\frac{1}{\left(\frac{1}{4n_V} + \frac{1}{n_{eon}}\right)} \tag{2.19}$$

In many cases there is a significant difference of the concentrations of electronic and ionic defects. Hence, the chemical capacitance is determined by the minority charge carrier concentration (n_{min}) and equation 2.19 can be simplified to [49]:

$$C_{chem} \approx \frac{F^2 V}{RT} z_{min}^2 n_{min} \tag{2.20}$$

2.3 Electrochemical impedance spectroscopy

Electrochemical impedance spectroscopy is a powerful technique for the analysis of electrochemical systems. Advantages of this technique are the simplicity of the measurement setup, that the measurement itself is non-destructive and that it is possible to investigate phenomena whose relaxation times vary over many orders of magnitude. While the measurement itself is quite simple, the correct interpretation of the obtained impedance spectrum with respect to the underlying physical process often turns out to be quite challenging. A substantial element of interpreting an impedance spectrum is the fitting of the spectrum with a suitable equivalent circuit, which is discussed in section 2.3.2.

2.3.1 Working principle

In impedance spectroscopy the current (voltage) response to an applied alternating voltage (current) is measured. Thus, it is possible to distinguish resistive, capacitive and inductive phenomena. To simplify calculations and expressions, it is common to express quantities in complex notation with the imaginary unit j, as shown for voltage and current in equations 2.21a and 2.21b.

$$u = \hat{u} \cdot e^{j(wt+\phi_u)} \tag{2.21a}$$

$$i = \hat{i} \cdot e^{j(wt+\phi_i)} \tag{2.21b}$$

The impedance is calculated as follows:

$$Z(w) = \frac{\hat{u}}{\hat{i}} \cdot e^{j(\phi_u - \phi_i)} = \frac{\hat{u}}{\hat{i}} \cdot e^{j\phi} \tag{2.22}$$

The calculations for total impedances of serial and parallel connections rely on Kirchhoff's

laws, as it is demonstrated for two impedances in equations 2.23a and 2.23b, respectively:

$$Z = Z_1 + Z_2 \tag{2.23a}$$

$$Z = \frac{Z_1 \cdot Z_2}{Z_1 + Z_2} \tag{2.23b}$$

By applying an alternating voltage, resistive and/or capacitive responses are obtained. In the field of electrochemistry inductive effects are often of minor importance. Resistive effects can be attributed to the movement of charge carriers or to electrochemical reactions. In the latter case, due to the applied alternating voltage the electrochemical reaction is driven back and forth around its equilibrium and the obtained resistance characterises the reaction rate. Capacitive effects may result from the charging of double layers or from chemical capacitances. Different charge carriers are present in mixed ionic-electronic conductors, as described in section 2.2, the concentration of these charge carriers can be shifted by an applied voltage, which causes a capacitive response that is referred to as the chemical capacitance. The impedance of a resistor and a capacitor is given by equations 2.24a and 2.24b.

$$Z_R = R \tag{2.24a}$$

$$Z_C = \frac{1}{jwC} \tag{2.24b}$$

The frequency dependent impedance can be visualised with a so called Nyquist plot, where the imaginary part of the impedance is plotted against its real part as it is shown in Figure 2.2. Each data point in Figure 2.2 has a different frequency and the frequency decreases from left to right. The frequency at the apex of the semicircle represents the relaxation frequency w_p, see equation 2.25.

$$w_p = \frac{1}{RC} = \frac{1}{\tau_p} \tag{2.25}$$

In equation 2.25 τ_p is the relaxation time, that can be interpreted as the time needed for a physical process to respond to a system disturbance.
The behaviour of capacitances is often not ideal, e.g. due to inhomogeneities. This non ideal behaviour is considered by using a constant phase element (CPE) instead of a capacitor. The impedance of a constant phase element is given by equation 2.26a. Q is the CPE parameter and the CPE exponent n quantifies the non ideal behaviour of the CPE. If $n = 1$ the constant phase element is an ideal capacitor. Equation 2.26b shows how the

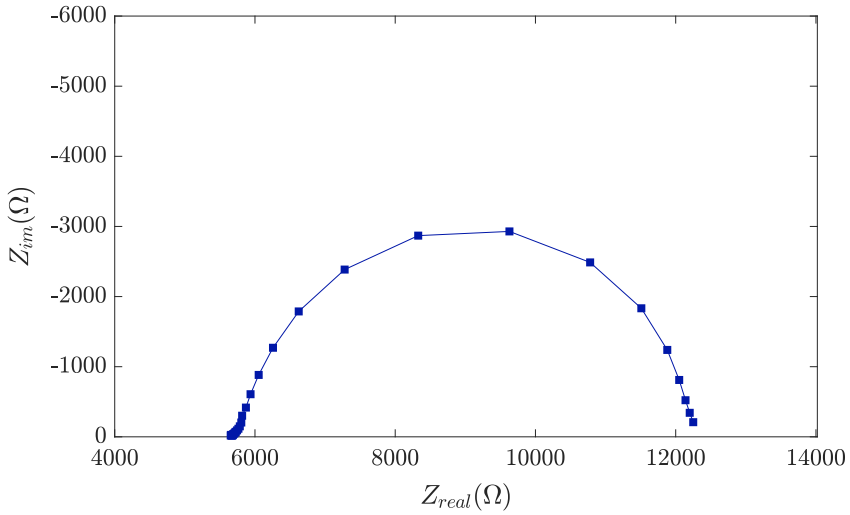

Figure 2.2: Example of a Nyquist plot

capacitance of a constant phase element is calculated.

$$Z_{CPE} = \frac{1}{(jw)^n Q} \tag{2.26a}$$

$$C = (R^{1-n} \cdot Q)^{\frac{1}{n}} \tag{2.26b}$$

2.3.2 Equivalent circuits

Electrochemical impedance spectroscopy is often used in order to investigate electrical and dielectric properties of mixed conducting oxides. Measured impedances can be analysed quantitatively by fitting the obtained impedance spectra with a suitable equivalent circuit using the complex nonlinear least square method and extracting the resulting parameters. In addition, a mechanistic evaluation might also be possible if the equivalent circuit is based on a physical process.
Jamnik and Maier [48] developed a generalised equivalent circuit model for mixed ionic-electronic conductors. An equivalent circuit for LSC on a YSZ electrolyte based on the model developed by Jamnik and Maier is shown in Figure 2.3a. This equivalent circuit can be further simplified. Since LSC is a mixed conductor with relatively high electronic conductivity, the electronic resistors R_{eon} can be neglected and the electronic rail is short

circuited. Additionally, the transport in LSC is surface controlled assuming thin film geometry and sufficient ionic conductivity. Therefore, the ionic transport resistances in LSC R_{ion} vanish and the chemical capacitors c_{chem}, which are all in parallel, can be replaced by a single chemical capacitance C_{chem}. Since the reaction is surface controlled, R_s represents the surface exchange resistance. R_s is in parallel with the surface capacitance $C_{s,ion}$. The remaining circuit elements are the ionic transfer resistance $R_{LSC|YSZ}$ and the capacitance $C_{LSC|YSZ}$ due to electron blockage at the interface between LSC and YSZ. The ionic transport through the electrolyte is taken into account with the resistance R_{YSZ}.
The equivalent circuit resulting from the above mentioned simplifications is shown in Figure 2.3b. Another simplification can be applied by neglecting the surface capacitance $C_{s,ion}$ because of its minor contribution compared to the usually big chemical capacitance C_{chem}.

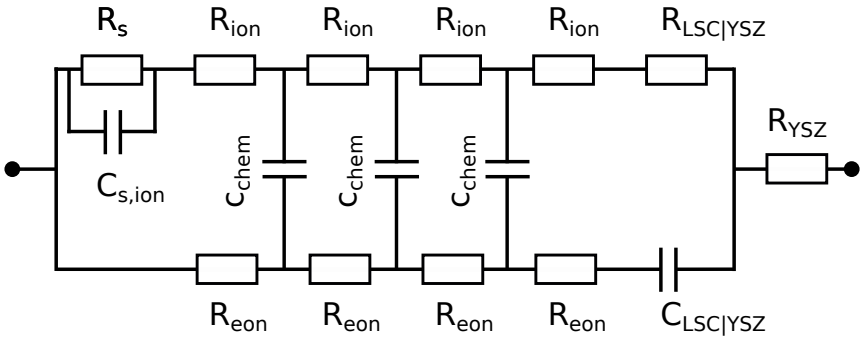

(a) General equivalent circuit

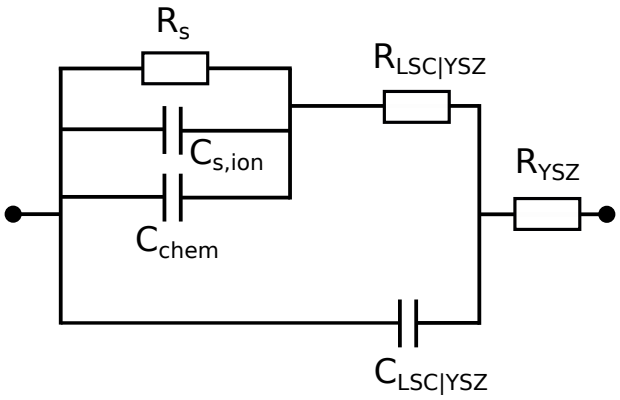

(b) Simplified equivalent circuit

Figure 2.3: General equivalent circuit for LSC on a YSZ electrolyte (a) and the simplified equivalent cricuit assuming high electronic and ionic conductivity and surface controlled transport in LSC (b)

2.3.3 Impedance measurements with DC bias

As described in section 2.3.1 an electrochemical reaction is driven back and forth around its equilibrium by applying an alternating voltage. If an additional DC bias voltage U_{DC} is applied, this equilibrium is shifted, which causes an additional net reaction rate and therefore an additional net DC current. Figure 2.4 shows the current-voltage curve of an arbitrary electrochemical reaction and the ranges that are investigated with impedance spectroscopy by applying an alternating voltage with and without bias.

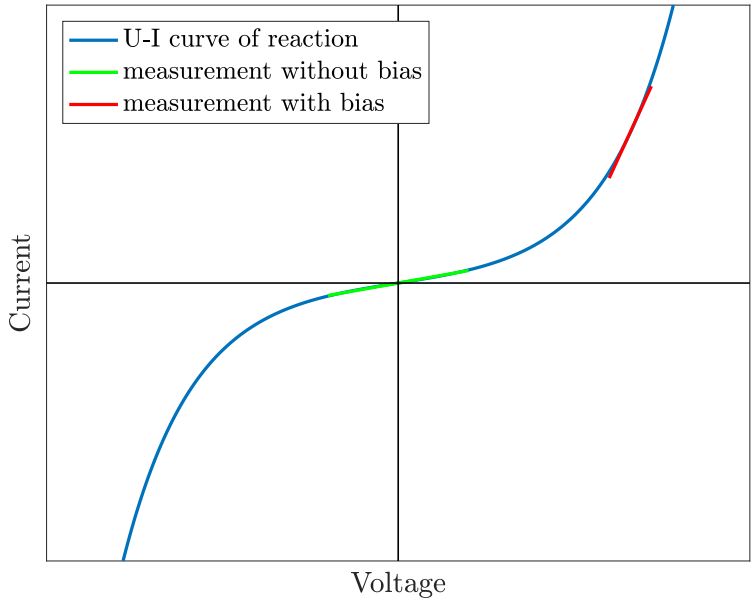

Figure 2.4: Current-voltage characteristic of an electrochemical reaction

In order to understand the consequences of an applied DC bias voltage, it is necessary to consider the electrochemical potentials of the different components of a cell. Therefore, a cell is assumed with a counter electrode (CE) and a working electrode (WE) consisting of a mixed ionic-electronic conducting material and an oxygen ion conducting electrolyte between these electrodes.
The electrochemical potential of oxygen $\tilde{\mu}_O$ in an oxide electrode is determined by the electrochemical potentials of electrons $\tilde{\mu}_e$ and oxygen ions $\tilde{\mu}_{O^{2-}}$, see equation 2.27 . An ideal counter electrode is always in equilibrium with the gas phase, consequently the electrochemical potentials of oxygen, oxygen ions and electrons are fixed regardless of the applied DC voltage.

$$\tilde{\mu}_O = \tilde{\mu}_{O^{2-}} - 2 \cdot \tilde{\mu}_e \tag{2.27}$$

The applied DC bias voltage U_{DC} leads to a difference in the electrochemical potentials of electrons between the working and the counter electrode:

$$\Delta\tilde{\mu}_e = F \cdot U_{DC} \tag{2.28}$$

Within the electrodes it can be assumed that $\tilde{\mu}_e$ is constant due to the high electronic conductivity of MIECs. The finite ionic conductivity of the electrolyte causes a change of the electrochemical potential of oxygen ions across the electrolyte. This change can be expressed with the DC current I_{DC} and the ionic transport resistance R_{YSZ} of the electrolyte as it is shown in equation 2.29a. This loss across the electrolyte is a part of the applied DC voltage and is referred to as the Ohmic overpotential, see equation 2.29b.

$$\Delta\tilde{\mu}_{O^{2-}} = 2 \cdot F \cdot \eta_{YSZ} \tag{2.29a}$$

$$\eta_{YSZ} = I_{DC} \cdot R_{YSZ} \tag{2.29b}$$

Due to the changes $\Delta\tilde{\mu}_e$ and $\Delta\tilde{\mu}_{O^{2-}}$ across the cell, there is also a change in the oxygen electrochemical potential:

$$\Delta\tilde{\mu}_O = \Delta\tilde{\mu}_{O^{2-}} - 2 \cdot \Delta\tilde{\mu}_e \tag{2.30}$$

As a result, the working electrode is not in equilibrium with the oxygen partial pressure of the gas phase. The described difference in the electrochemical potential of oxygen is also a part of the applied DC voltage. This part is called the overpotential of the working electrode η_{WE}. Assuming no losses in the counter electrode, η_{WE} can be expressed as follows:

$$\eta_{WE} = U_{DC} - \eta_{YSZ} = U_{DC} - I_{DC} \cdot R_{YSZ} \tag{2.31}$$

By defining an equivalent oxygen partial pressure p_{equi} inside the working electrode, this overpotential can be described with the Nernst equation according to:

$$\eta_{WE} = \frac{RT}{2F} \cdot ln\left(\frac{p_{equi}}{p_{act}}\right) \tag{2.32}$$

Here, R is the universal gas constant, F the Faraday constant and T the temperature. Furthermore, p_{act} is the actual atmospheric oxygen partial pressure. With this definition, the equivalent oxygen partial pressure determines the defect chemical state of the working electrode and can be expressed as:

$$p_{equi} = p_{act} \cdot e^{\frac{\eta_{WE} 2F}{RT}} \tag{2.33}$$

Thus, the equivalent oxygen partial pressure and therefore the defect chemical state is controlled by the actual atmospheric oxygen partial pressure and the applied bias voltage.

3 Experimental methods

3.1 Sample preparation

All samples were prepared using the same procedure. For the fabrication of the working electrodes, LSC thin films were deposited on YSZ single crystals using pulsed laser deposition (PLD). The next step included microstructuring via photolithography and ion beam etching. The counter electrodes were prepared by depositing LSC on the back side of the samples with different deposition parameters, so that a porous thin film was obtained. Details of these production steps are explained in the following sections.

3.1.1 Pulsed laser deposition

LSC thin films were deposited onto YSZ (100) single crystals (9.5 mol % Y_2O_3, Crystec Germany), which were polished on one side, had a thickness of 0.5 mm and a size of 5x5 mm^2. The films for the working electrode were deposited on the polished side of the crystals. The $La_{0.6}Sr_{0.4}CoO_{3-\delta}$ targets for the deposition were previously prepared via Pechini synthesis. Ablation of the targets was done in a vacuum chamber using a KrF excimer laser (Complex Pro 201F) with a wavelength of 248 nm. Prior to the ablation of the targets, the chamber was evacuated to 10^{-4} mbar, then the oxygen partial pressure was adjusted. The samples were heated to the desired deposition temperature, which was measured with a pyrometer adjusted for the emissivity of YSZ. The laser was operated with a pulse rate of 5 Hz with an energy of 400 mJ per pulse. After the deposition, the samples were cooled down with a cooling rate of 15 °C per minute. The oxygen partial pressure, the target-sample distance and the sample temperature varied depending on whether thin films were deposited for the working or the counter electrodes. The deposition parameters for both electrodes are summarised in Table 3.1.

3.1.2 Microstructuring

After the deposition of the thin LSC film working electrodes, microstructuring was done via photolithography and ion beam etching. Each step of the microstructuring process is

Table 3.1: Parameters used for pulsed laser deposition of thin film working and counter electrodes

PLD parameters		
	Working electrode	Counter electrode
Laser wavelength (nm)	248	248
Laser pulse rate (Hz)	5	5
Laser energy per pulse (mJ)	400	400
Deposition time (min)	30	30
Sample temperature (°C)	600	450
Oxygen partial pressure (mbar)	0.04	0.4
Target-sample distance (cm)	6	5

shown in Figure 3.1. The samples were taken to a dust-free cleanroom, where the photolithography was done. Before coating the samples with a photoresist, they were cleaned with nitrogen gas. Then the samples were coated with 3x100 µl of photoresist (ma-N 1420 MicroResist Technology, Germany) using a spincoater (SCC-200 KLM, Germany), spinning the samples every 100 µl for 1 min. After heating the samples in order to evaporate the excess solvent, they were exposed to UV light (350 W, USHIO 350DP Hg, Ushio, Japan) through a patterned shadow mask to obtain circular microelectrodes with diameter of 195 - 300 µm. The non-illuminated parts of the photoresist were removed with a developer solution (ma-D 533/s, MicroResist Technology, Germany) and thereafter the samples were cleaned with deionised water. All parameters of the photolithography process are shown in Table 3.2. The uncovered areas of LSC were now removed via ion beam etching. The samples were placed into a vacuum chamber with thermally conductive paste on the back side of the samples to prevent overheating due to the ion beam. The etching was done by using a diffuse Ar plasma. The rim of the surface with the LSC thin film was not etched, because of the thick polymer layer at this rim which originated from the spincoating. The parameters for the ion beam etching can be found in Table 3.3. Finally, the remaining photoresist was removed with a clean room wipe, which was soaked in ethanol. To determine the size of the microelectrodes, their diameter was measured with a light microscope (Zeiss, Germany).
The first sets of microelectrodes were fabricated using only 100 µl of photoresist. For some

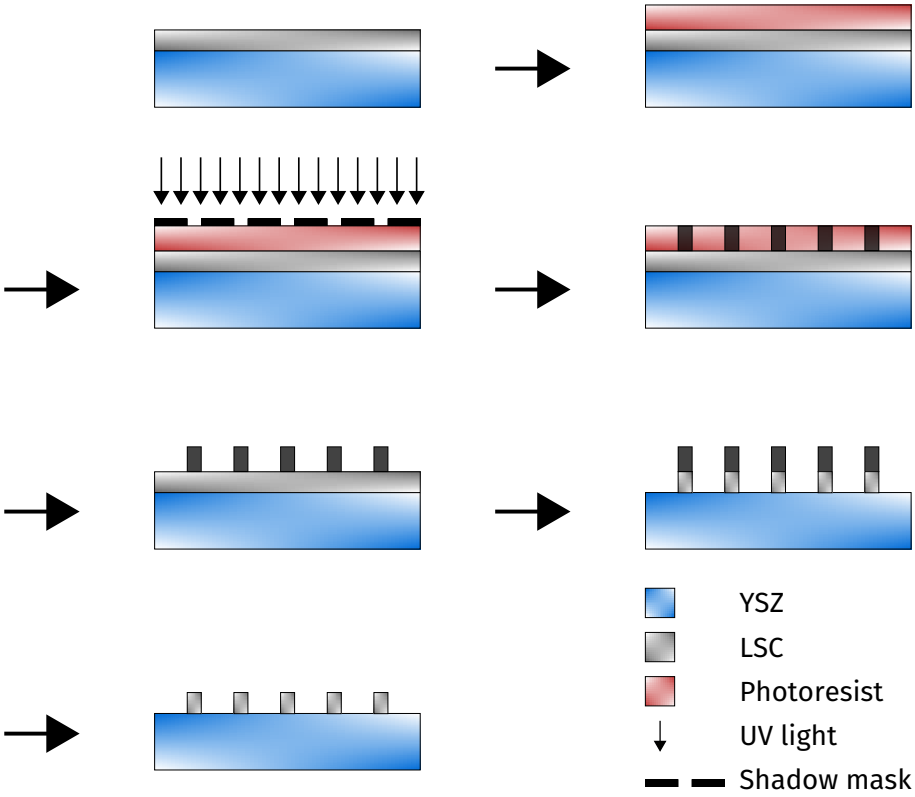

Figure 3.1: Workflow of the microstructuring

microelectrodes of these samples it was not possible to remove the remaining photoresist after the ion beam etching, neither with a clean room wipe soaked in ethanol nor with acetone and isopropanol. It was also tried to remove the photoresist by leaving the samples in glasses with ethanol, acetone or isopropanol for 24 hours. Even if these glasses with the samples inside were taken to an ultrasonic bath for 30 minutes, the photoresist was still remaining on the microelectrodes. This behaviour most likely resulted from a reaction between the photoresist and the LSC during the ion beam etching due to overheating of the samples. This problem no longer appeared with the use of 3x100 µl of photoresist. Figure 3.2a shows a microelectrode, on which it was not possible to remove all of the photoresist, whereas a microelectrode without any photoresist is shown in Figure 3.2b.

Table 3.2: Parameters used for photolithography

Photolithography parameters	
Photoresist volume (µl)	300
Spincoater speed (rpm) / duration (s)	75 / 45 and 30 / 10
Heating temperature (°C)	105
Heating duration (min)	10
Exposure time to UV light (s)	60
Developing time (s)	90 to 120

Table 3.3: Parameters used for ion beam etching

Ion beam etching parameters	
Argon pressure (mbar)	$1.4 \cdot 10^{-4}$
Plasma current (mA)	0.9 to 1.9
Etching time (min)	90 to 150
Beam voltage (kV)	3
Extractor voltage (kV)	3
Magnetron current (mA)	25

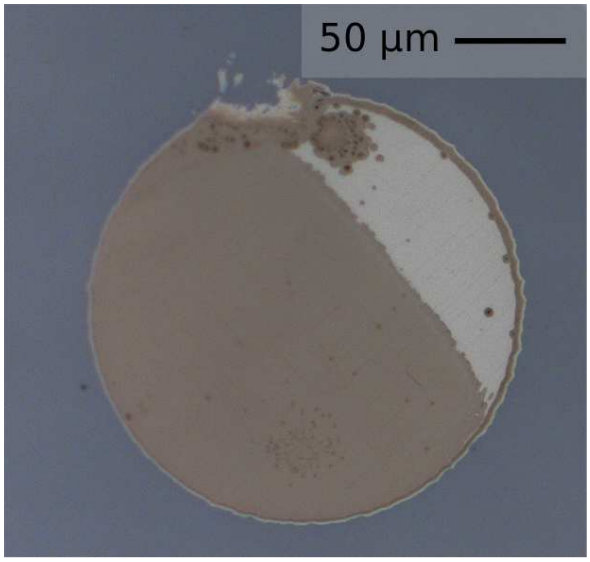

(a) Microelectrode with non removable photoresist

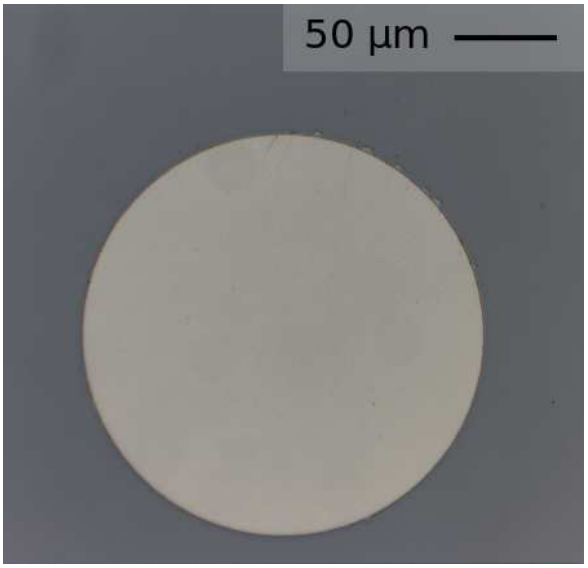

(b) Microelectrode with no remaining photoresist

Figure 3.2: Microelectrodes, where 100 µl (a) or 3x100 µl (b) of photoresist was used in the photolithography process

3.2 Sample characterization

3.2.1 Scanning electron microscopy

The surface morphology of the samples was analysed by scanning electron microscopy (SEM) carried out at the USTEM (TU Wien) using a FEI Quanta 250 FEGSEM. Due to the insulating electrolyte, the microstructured thin films had to be coated with a thin gold layer in order to obtain sufficient electronic conductance. The surface morphology was investigated using secondary electron images.

3.2.2 X-ray diffraction

LSC thin film microelectrodes were examined by means of X-ray diffraction (XRD) measurements with an Empyrean X-ray diffractometer (Malvern Panalytical) equipped with a focusing mirror on the incident beam side and a semiconductor area detector (GaliPIX3D) on the diffracted beam side. A Cu-K_α radiation and Bragg Brentano geometry was used for all measurements. In order to focus the beam on individual microelectrodes with a diameter of about 195 µm, a 0.3 mm slit was used. The diffractograms were evaluated with Panalytical Highscore.

3.2.3 Profilometry

A DektakXT profilometer (Bruker, USA) provided with a diamond equipped stylus with a vertical resolution of 0.1 nm and a stylus force of 10 mg was used to measure the thickness of the thin films. Small dots of platinum paste were applied to a YSZ substrate prior the deposition of LSC at the usual parameters. These small dots were removed with ethanol afterwards, which led to holes in the LSC thin film. The thickness of the electrodes was obtained by measuring the depth of these holes with the profilometer.

3.3 Electrochemical impedance spectroscopy

3.3.1 Measurement setup

The measurement setup for the impedance measurements is shown in Figure 3.3. The samples were placed on a heating stage in a vacuum chamber, which shielded the sample against electrical interferences caused by surrounding instruments. For the first set of impedance measurements, a Limkam® Scientific heating stage was used. A prebaked platinum paste was used to connect the counter electrodes with the non-etched rim of the LSC thin films. These platinum dots at the rim of the LSC thin films were then contacted

with platinum needles, which were clamped by a gold coated steel tip of a micromanipulator. For the second set of impedance measurements a new corundum heating stage was used, which was coated with platinum, see Figures 3.3 and 3.4. The electrical contact was ensured by a platinum wire which was connected to the platinum coated surface of the heating stage. This platinum wire was surrounded by corundum and again connected to a gold coated steel tip of a micromanipulator. In order to contact the working (micro-) electrodes, a platinum needle, which was also clamped by a tip of a micromanipulator, was used. Due to the small size of the measured microelectrodes, positioning of the needle was done with a movable micromanipulator, which was controlled by a software, and a microscope equipped with a camera. From the micromanipulators, cables led to the feedthrough out of the chamber. Besides a different applied set temperature to reach

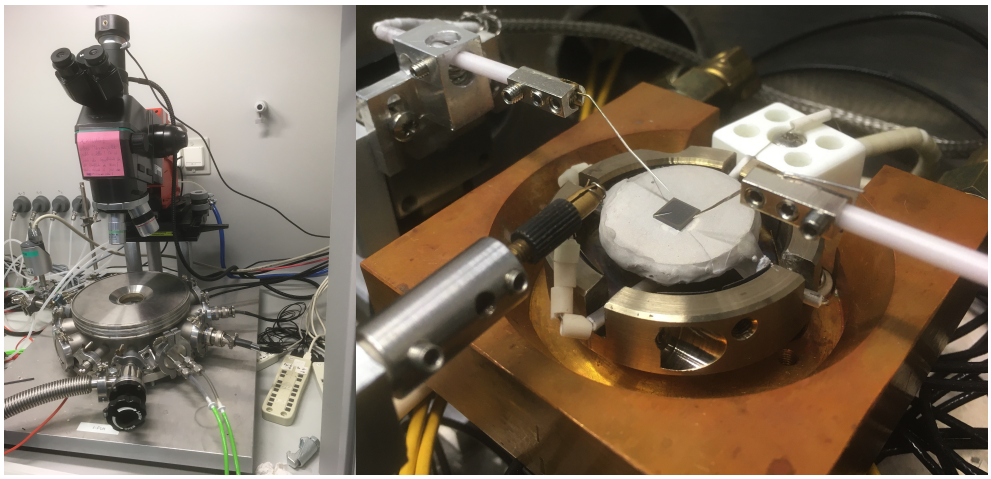

Figure 3.3: Measurement setup for the electrochemical impedance spectroscopy

similar microelectrode temperatures, no difference was observed between the two different heating stages. Set temperatures of 750 °C and 650 °C, respectively, led to microelectrode temperatures between 600 °C and 630 °C. The microelectrode temperature was calculated using the high frequency intercept in the impedance spectra which corresponds to the resistance R_{YSZ} of the ionic transport through the electrolyte [51]:

$$\sigma_{ion} = \frac{1}{2 d_{ME} R_{YSZ}} \tag{3.1a}$$

$$\sigma_{ion} = \sigma^0 \cdot e^{-\frac{E_a}{k_B T}} \tag{3.1b}$$

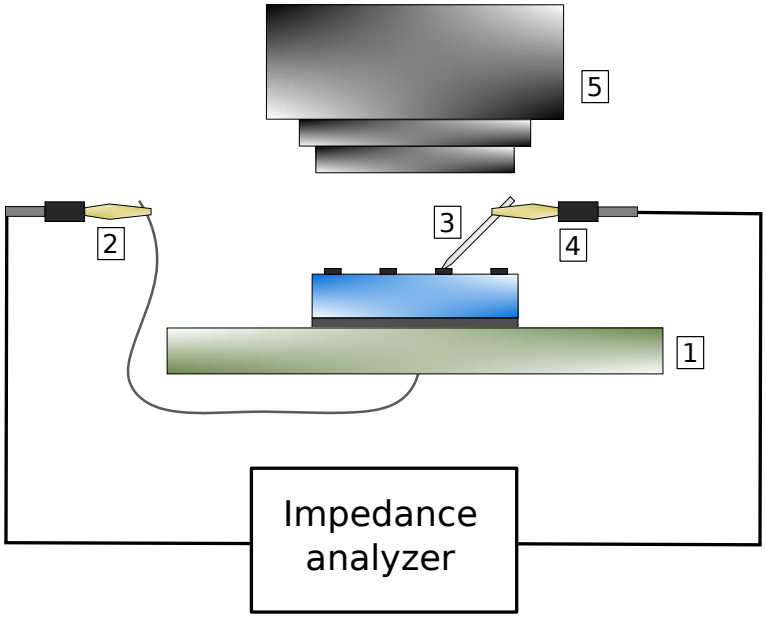

Figure 3.4: Measurement setup with the new heating stage: 1) platinum coated heating stage, 2) micromanipulator connected with counter electrode, 3) platinum needle, 4) movable micromanipulator, 5) microscope

$$T = \frac{0.767\,eV}{k_B \cdot ln(315.8\,\Omega^{-1}cm^{-1} \cdot d_{ME}R_{YSZ})} \tag{3.1c}$$

Here, d_{ME} stands for the diameter of the microelectrode, σ_{ion} denotes the ionic conductivity of YSZ and k_B is the Boltzmann constant. With σ^0 and the activation energy E_a being $157.9 \pm 16.3\,\Omega^{-1}\text{cm}^{-1}$ and 0.767 ± 0.007 eV, respectively, the temperature of microelectrodes can be calculated as it is shown in equation 3.1c. The deviation of the microelectrode temperature from the set temperature of the heating stage had two reasons, which are explained by Opitz et al. [51]. First, the samples were heated in an asymmetric way as it was only heated from below. Thus, a temperature gradient from the bottom to the top of the sample can be assumed. Second, the contact needles cooled the microelectrodes as they were clamped at a much lower temperature. Consequently, the contact needle acted as a heat sink. Further remarks to the microelectrode temperature and the cooling effect of the contact needles can be found in chapter 4.

All impedance measurements were carried out in synthetic air (99.999 %, Alphagaz), which was provided by two mass flow controllers with a flow of 10 sscm. Synthetic air was bubbled through the chamber for two hours prior heating in order to avoid reactions between the samples and possible contaminations in the lab air at elevated temperatures.

3.3.2 Impedance spectroscopy

For the impedance measurements with DC bias an Alpha-A High Performance Frequency Analyzer with an Electrochemical Test Station POT/GAL 30 V/2 A (Novocontrol Technologies GmbH & Co. KG, Germany) was used. An alternating voltage with an amplitude of 10 mV and an additional anodic DC voltage up to 1000 mV were applied. Impedance was measured in the frequency range of 1 MHz to 10 mHz with 5 data points per decade. DC voltages and currents were measured with the Electrochemical Test Station POT/GAL 30 V/2 A. In most of the measurements bias from 0 to 1000 mV was applied in cycles with bias steps of 20 to 50 mV. A cycle with increasing bias was followed by a cycle with decreasing bias and vice versa.

4 Results and discussion

4.1 Sample preparation

Circular LSC microelectrodes on a YSZ substrate were fabricated as described in section 3.1.2 via photolithography and ion beam etching, see Figure 4.1. Microelectrodes with a diameter between 195 - 350 µm were used for the impedance measurements.

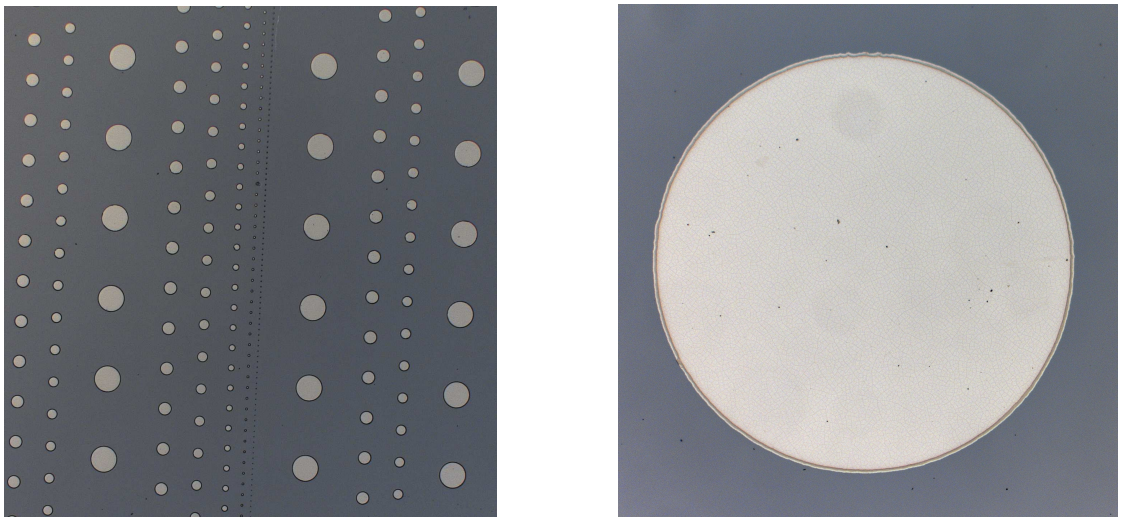

(a) Sample with microelectrodes of various sizes (b) Microelectrode with a diameter of 195 µm

Figure 4.1: Light microscope images of a pristine sample

The thickness of the microelectrodes was measured with a profilometer, see section 3.2.3. It turned out that if the samples were measured with the profilometer, thicknesses of the microelectrodes varied between 350 and 600 nm, although the parameters during the preparation were the same for all samples. It is assumed that inhomogeneities of the ion beam during the etching process are the reason for this. Four samples were all at once inside the chamber during the etching process. Therefore, these inhomogeneities could have led to a greater impact of the ion beam at some samples. Consequently, not only

LSC but also the underlying YSZ was removed around their microelectrodes, which led to greater thickness values in the profilometer measurement. However, measurements as described in section 3.2.3 revealed an electrode thickness of 350 nm. This thickness was used for all calculations in this work.

4.2 Electrochemical impedance measurements

4.2.1 Impedance spectra

Impedance measurements were performed in synthetic air with anodic DC voltage up to 1000 mV. The shape of the impedance spectra varied with the applied voltage and accordingly can be divided into 3 different groups. It was difficult to define a precise voltage range for these groups, due to the different behaviour of the samples and the smooth transition between the groups. Therefore, spectra with bias voltages up to 60 mV, sometimes even up to 150 mV, were attributed to the first group of impedance spectra. An example spectrum of this group is shown in Figure 4.2a. It contains an high frequency x-axis intercept, which corresponds to the ionic transport resistance in the YSZ electrolyte. Furthermore, the spectrum consists of a dominant low frequency semicircle that is attributed to the surface exchange resistance R_s and the chemical capacitance CPE_{chem} of the LSC microelectrode. The small shoulder at high frequencies, which can be seen in detail in Figure 4.2b, appears most likely due to the YSZ/LSC interface [52]. Spectra like the one in Figure 4.2a were fitted with a simple equivalent circuit consisting of a resistance and a R/CPE element in series. Contributions of the YSZ/LSC interface feature were neglected for the fit due to the much smaller impact compared to the surface exchange reaction.
The second group of impedance spectra is characterised by a distinctive linear slope at the high frequency onset of the semicircle that decreased with increasing bias voltage. This feature may be attributed to a transport limitation. Again it was not possible to define a precise voltage range for this group. An example spectrum assigned to the second group is shown in Figure 4.3a. Figure 4.3b shows the decrease of the slope with higher bias voltage. The high frequency x-axis intercept corresponds again to the transport resistance of the electrolyte. The equivalent circuit for the spectra of the second group consists of a resistance and two R/CPE elements in series. The additional R/CPE element was used to fit the feature in the intermediate frequency range. The second R/CPE element corresponds again to the surface exchange reaction. Impedances at the high frequency onset of the semicircle were not fitted, as can be seen from Figure 4.3b. Only one R/CPE element was used for the fit of second-group-spectra in order to investigate the chemical capacitance, see Figures 4.3c and 4.3d. As a consequence, the slope feature attributed to the transport limitation was neglected. Thus, it was possible to differentiate between

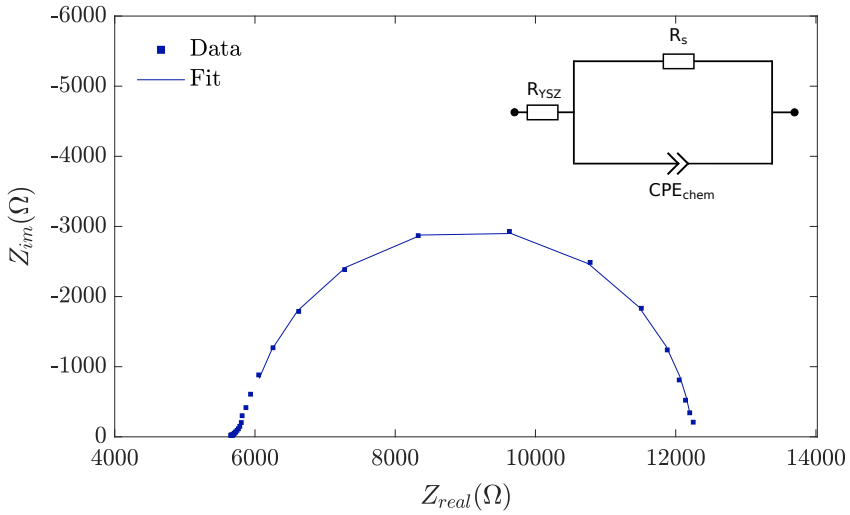

(a) Spectrum with no bias voltage

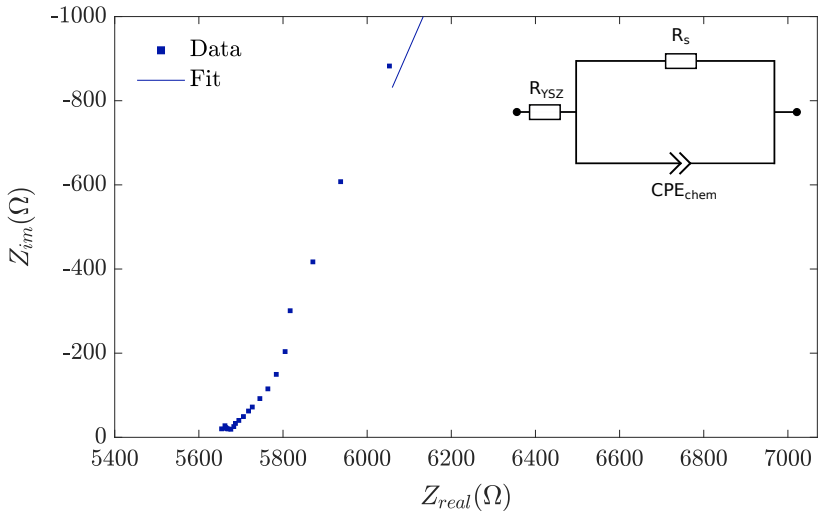

(b) High frequency shoulder of spectrum with no bias voltage

Figure 4.2: Impedance spectrum of a LSC microelectrode with 195 µm diameter and no applied bias voltage corresponding to the first group

individual features in these spectra and analyse the chemical capacitance quantitatively. For the third group the high frequency feature becomes more dominant with increas-

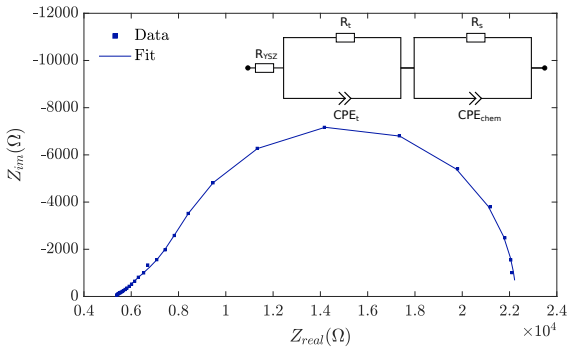

(a) Bias voltage of 320 mV

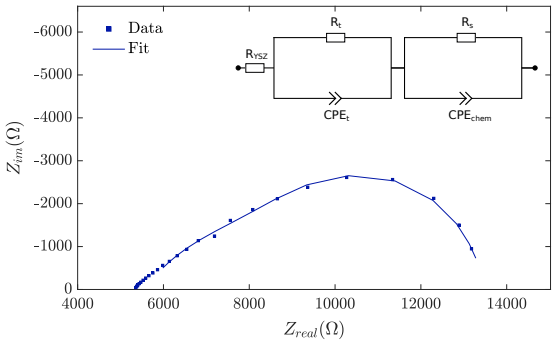

(b) Bias voltage of 400 mV

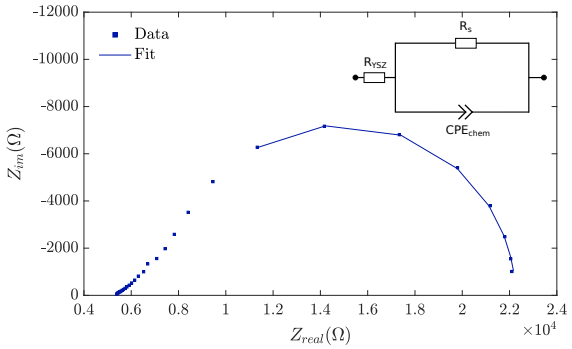

(c) Bias voltage of 320 mV with corresponding fit used to obtain the chemical capacitance

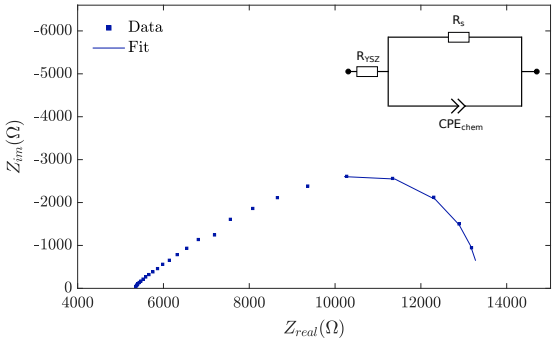

(d) Bias voltage of 400 mV with corresponding fit used to obtain the chemical capacitance

Figure 4.3: Impedance spectra of a LSC microelectrode with 195 µm diameter with different applied bias voltages corresponding to the second group

ing bias voltage, whereas the semicircle attributed to the surface exchange gets smaller with increasing bias voltage until it is not identifiable anymore. This results in flattened impedance spectra and a decreasing resistance with increasing bias voltage. The described evolution can be seen in Figures 4.4a - 4.4d. The same equivalent circuit as for the second group was used as long as the features were reasonably distinguishable (Figures 4.4a and 4.4b). At higher bias voltages an equivalent circuit with a resistance and a single R/CPE element was used for the fit of the flattened impedance spectra (Figures 4.4c and 4.4d). Since porous counter electrodes that were fabricated with the parameters described in section 3.1.1 showed excellent performance in previous studies [53] and their area was at least 250 times larger than that of the microelectrodes, its influence on the impedance

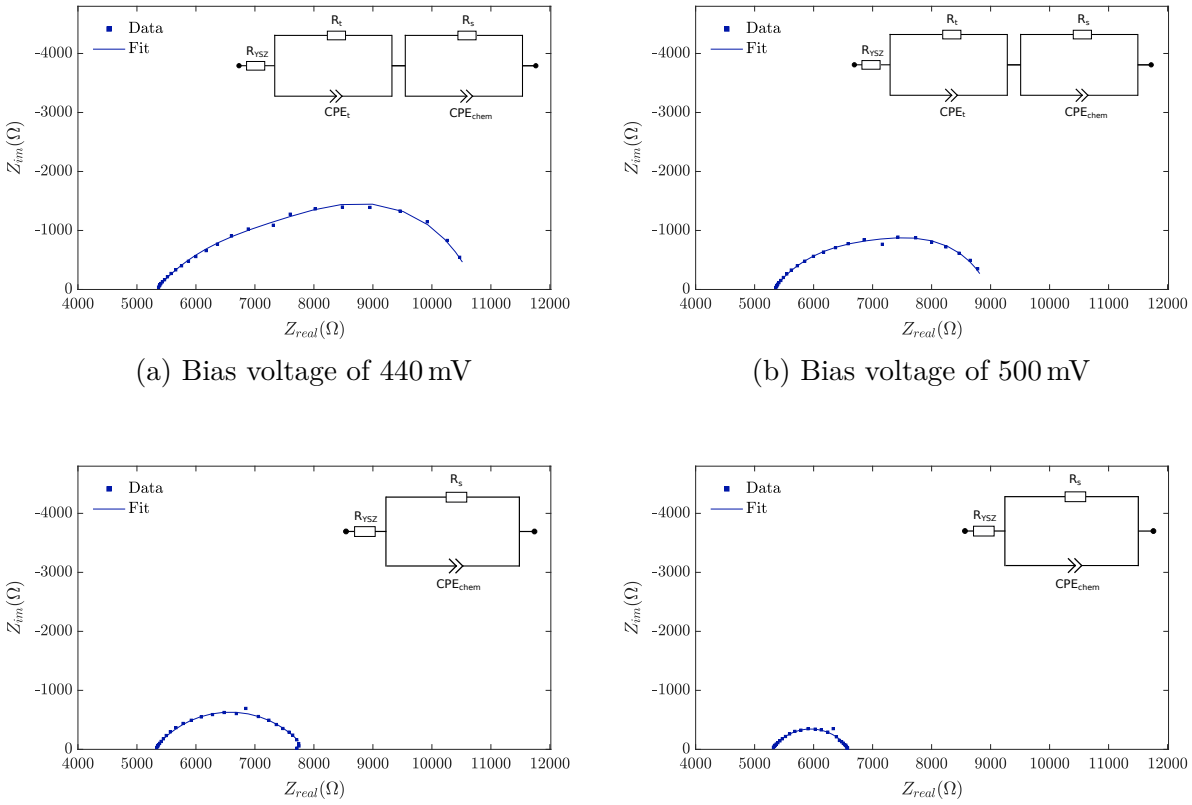

(a) Bias voltage of 440 mV

(b) Bias voltage of 500 mV

(c) Bias voltage of 600 mV

(d) Bias voltage of 1000 mV

Figure 4.4: Impedance spectra of a LSC microelectrode with 195 µm diameter with different applied bias voltages corresponding to the third group

spectra was neglected.

4.2.2 Oxygen exchange kinetics

In order to investigate the oxygen exchange kinetics of the LSC microelectrodes, resistance-overpotential and current-overpotential curves were analysed. The resistances were determined by fitting the obtained impedance spectra with suitable equivalent circuits, which were described in section 4.2.1, and extracting the resistance values of the semicircle associated with the electrode resistance. Hence, this resistance included the surface exchange resistance R_s and the resistance attributed to the transport limitation R_t. The overpotential of the microelectrodes was calculated as explained in section 2.3.3:

$$\eta_{WE} = U_{DC} - \eta_{YSZ} = U_{DC} - I_{DC} \cdot R_{YSZ} \tag{4.1}$$

In equation 4.1, U_{DC} and I_{DC} are the DC voltage and current, which were measured with the Electrochemical Test Station POT/GAL 30 V/2 A. The ionic transport resistance of YSZ, R_{YSZ}, was determined by extracting the real part of the impedance at the high frequency x-axis intercept.

Kinetics of pristine electrodes

In the first experiments, pristine electrodes were used and DC voltages were applied in cycles from 0 to 1000 mV and 1000 to 0 mV, respectively. Figure 4.5a shows that four bias cycles were applied with bias steps of 20 mV between each measurement. The corresponding current-overpotential and resistance-overpotential curves can be seen in Figures 4.5b and 4.5c. The open circuit oxygen exchange resistance shown in Figure 4.5c is about 2 Ωcm^2 at 600 °C (calculated from R_{YSZ}), which is in accordance with values from the work of Rupp et al. [53]. The course of the resistance showed a slight increase within the first three bias steps of the first cycle, which is most likely attributed to degradation effects. However, with increasing bias the resistance remains almost constant until a significant increase appears starting at an overpotential of about 110 mV. This increase leads to a strong peak with a maximum resistance of 5.2 Ωcm^2 at an overpotential of 257 mV. In Figure 4.5b it can be seen that the DC current increases strongly within the first three to four bias steps before the curve becomes rather flat at that range of overpotential where there is the strong peak of the resistance. This increase within the first bias steps shows linear behaviour as can be seen in Figure 4.5d. Starting from approximately 300 mV overpotential, the current increases significantly and therefore the resistance drops. This strong activation of the microelectrode at the end of the first bias cycle results in a minimum of the oxygen exchange resistance of about 0.4 Ωcm^2. The highest applied bias of 1000 mV corresponds to an overpotential of about 385 mV because most of the bias drops across the

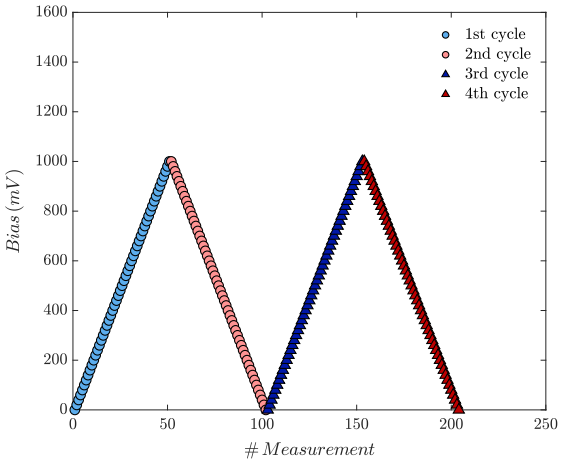

(a) Applied bias over the measurement course

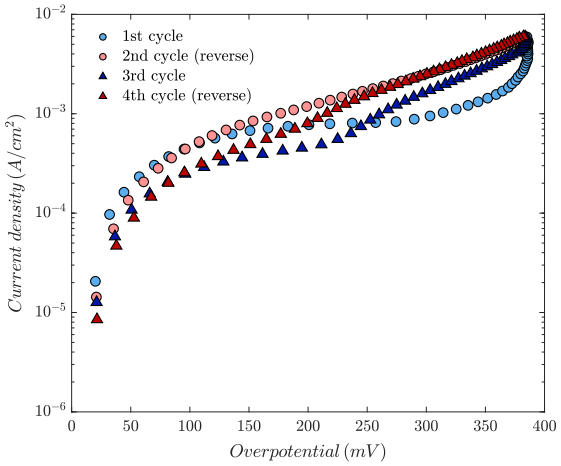

(b) Current-overpotential curve

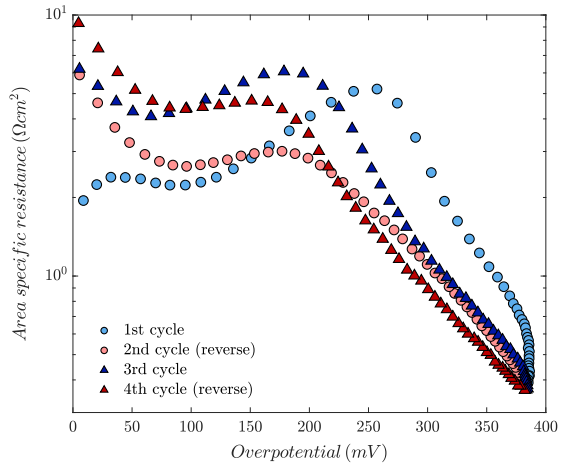

(c) Resistance-overpotential curve

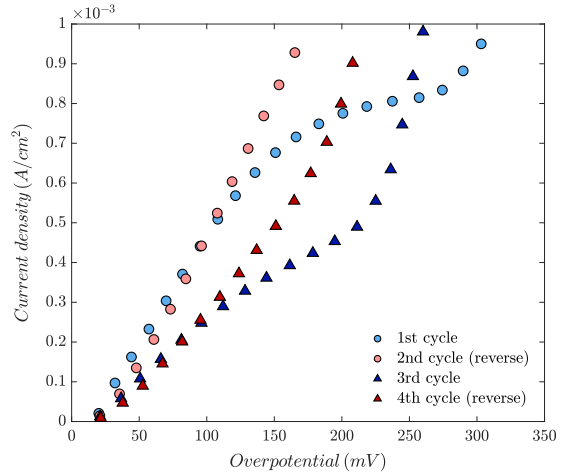

(d) Linear plot of current-overpotential curve

Figure 4.5: Measurements on a pristine microelectrode with a diameter of 195 µm at a measurement temperature of 600 °C

electrolyte.
The strong activation at the end of the first cycle leads to an increased current in the second cycle, where bias was applied in reverse from 1000 to 0 mV. Now the current decreases until values are similar to those of the first cycle at about 100 mV overpotential. At lower

overpotentials the current drops similarly as in the first cycle. The resistance increases at a constant rate until a plateau is reached at about 200 mV. The plateau is followed by a slight decrease until the resistance increases again starting from approximately 75 mV. The open circuit resistance at the end of the second cycle is more than twice as high as the one of the first cycle. This degradation of the surface related resistance is most likely caused by compositional changes of the LSC thin film. Kubicek et al. [54] showed that annealing at 600 °C leads to segregation of strontium to the surface of $La_{0.6}Sr_{0.4}CoO_{3-\delta}$ thin films which causes the increase in oxygen exchange resistance. Thus, it is assumed that strontium segregation to the surface is also the main reason for the degradation of the electrodes investigated in this work.
In the third cycle the bias was applied from 0 to 1000 mV as in the first cycle. It starts with a decrease of the resistance and therefore an increase of the current with increasing anodic overpotential. A peak of the resistance is obtained, but with a minor increase and at a lower overpotential (200 mV) compared to the peak in the first cycle. The current-overpotential levels after the initial increase, but at lower values than in the first cycle. Furthermore, there is now a slope of the current at about 250 mV which is followed by a linear increase. This corresponds to a linear decrease of the resistance similar to the curve of the second cycle. Although the slope of the resistance as well as of the current is lower, the minimum value of the resistance is the same as in the first cycle.
Both the resistance-overpotential and the current-overpotential curves of the fourth cycle are similar in shape to those of the second cycle. However, the open circuit resistance of the fourth cycle is increased due to the ongoing degradation. The reason for the peaks of the electrode resistance in the forward (first and third) cylces is still unclear, therefore further investigations are needed. This complex behaviour of a pristine electrode was reproducibly measured, a second series is shown below (*Kinetics after annealing at 700 °C*).

Kinetics of electrodes with a thermal history

Samples, which already had a thermal history at the beginning of the measurement were used in order to investigate kinetics of degraded electrodes upon anodic polarisation. Therefore, bias cycles were applied in the same way as for the pristine electrodes (Figure 4.6a). Figure 4.6c shows the degradation of an electrode with a thermal history of 6 h at 630 °C as the open circuit resistance is about 60 Ωcm^2 compared to 2 Ωcm^2 for the pristine electrode. Moreover, there is no peak in the resistance of the first and the third cycle as it was the case for the pristine electrode. The oxygen exchange resistance remains almost constant in the first cycle with increasing overpotential before it starts to decrease at about 160 mV. The corresponding current of this overpotential range is shown in Figure 4.6d. The decrease of the resistance starts at a lower overpotential than the drop in the

resistance obtained for the pristine electrode. In Figure 4.6b the corresponding increase of the current is shown. The slope of the current becomes steeper at an overpotential of about 250 mV, which is associated with a change of the resistance slope at the same overpotential. At the end of the first cycle the current increases strongly and therefore the resistance drops similar to the curves of the pristine electrode. Due to the different shape of the curves in the first cycle compared to the pristine electrode, it can be assumed that different mechanisms are involved for degraded electrodes.
From Figures 4.6c, 4.6b and 4.5c, 4.5b it can be seen that the shape of the resistance-overpotential and the current-overpotential curves of the second, third and fourth cycle of the degraded electrode are similar to the curves of the pristine electrode (Figures 4.6c and 4.6b). It is noticeable, that the current of the reverse (second and fourth) cycles is always higher than for the forward cycles (first and third). This indicates that the effect of the strong activation at the end of the forward cycles remains for a certain time and thus increases the current and decreases the resistance. The activation upon anodic polarisation is also demonstrated by the lower open circuit resistances in the second, third and fourth cycle of the degraded electrode.

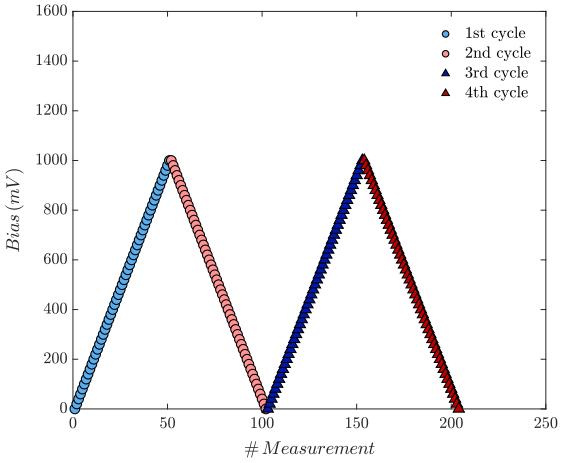

(a) Applied bias over the measurement course

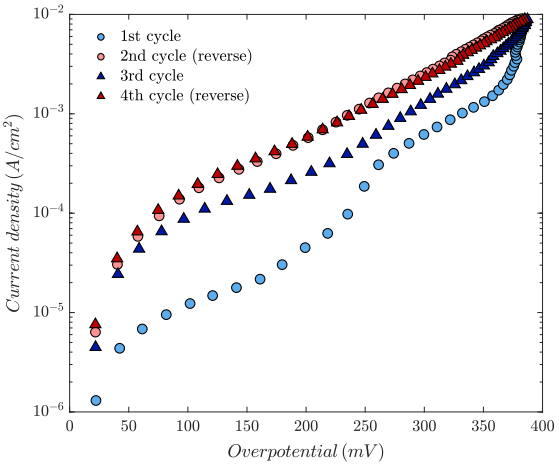

(b) Current-overpotential curve

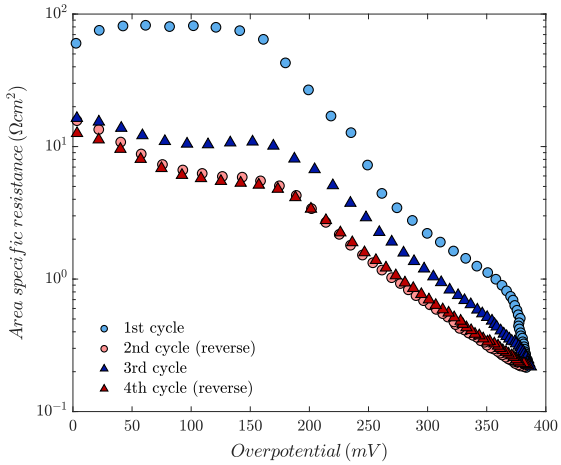

(c) Resistance-overpotential curve

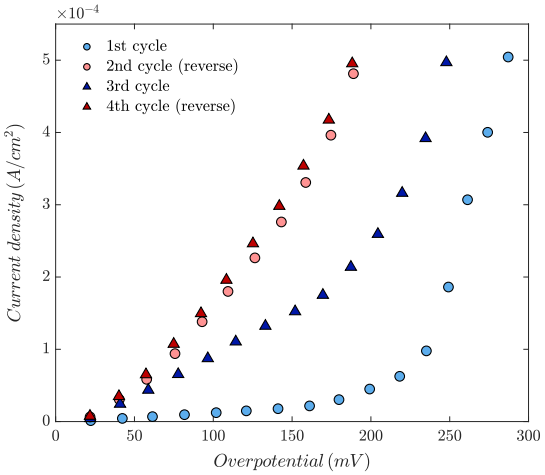

(d) Linear plot of current-overpotential curve

Figure 4.6: Measurements on a microelectrode with a diameter of 195 µm and a thermal history of 6 h at the measurement temperature of 630 °C

Kinetics after annealing at 700 °C

Samples were heated to a temperature of 700 °C for 2 h after measuring four bias cycles with bias steps of 40 mV (corresponding to 22.5 h). The effect of annealing on kinetics of the LSC electrodes was investigated by performing two more bias cycles immediately after the 2 h at 700 °C (Figure 4.7a). The behaviour of the resistance-overpotential and the current-overpotential curves (Figures 4.7b, 4.7c and 4.7d) of the first four cycles is similar to the previously shown behaviour of a pristine electrode (Figures 4.5c and 4.5b), which indicates the reproducibility of these measurements. After 2 h of annealing at 700 °C, the open circuit resistance shows a significantly higher value, which may be attributed to an enhanced Sr segregation to the surface due to annealing. The shape of the curves of the fifth (first after annealing) cycle is similar to that of the first cycle of the degraded electrode (Figures 4.6c and 4.6b). This already suggests, that deviations from pristine samples are mainly an effect of the thermal history. It is shown, that the strong activation and the resulting higher current in the following reverse bias cycle, still occurs even after annealing at a higher temperature.

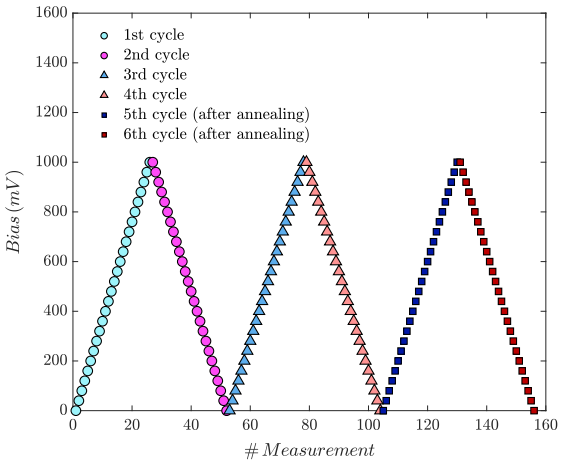

(a) Applied bias over the measurement course

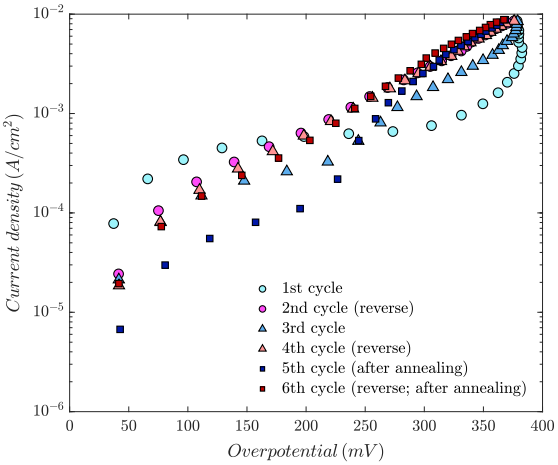

(b) Current-overpotential curve

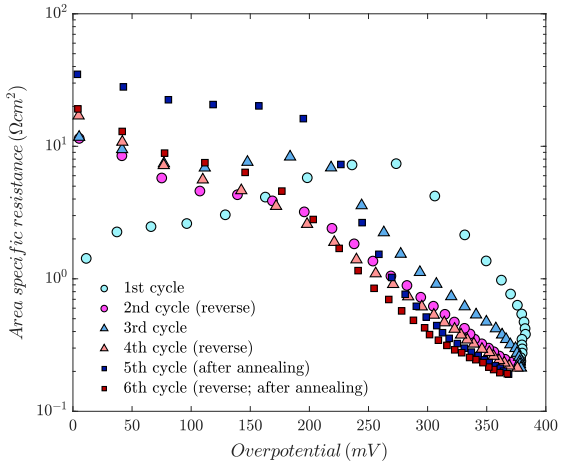

(c) Resistance-overpotential curve

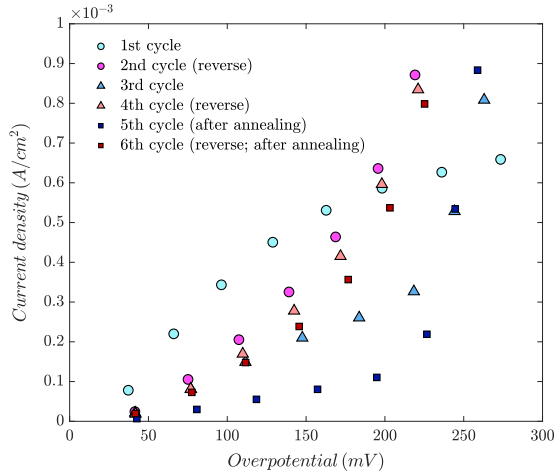

(d) Linear plot of current-overpotential curve

Figure 4.7: Measurements on a pristine microelectrode with a diameter of 195 µm at a measurement temperature of 626 °C; annealing for 2 h at a sample temperature of 700 °C was performed after the fourth bias cycle

Bias cycles with lower DC voltage

Kinetics of electrodes were also probed with bias cycles containing maximum DC voltages of 200 mV, see Figure 4.8a. The current-overpotential curve (Figures 4.8b and 4.8d) of the first cycle shows a significant increase within the first bias steps before it levels, just as it was shown before in the case of pristine electrodes. However, with the omission of higher DC voltages, there is no activation and thus, the reverse cycles do not show an increased current. The resistance slightly increases for the first two to three bias steps in the first and third cycle, which is again most likely due to degradation effects (Figure 4.8c). With increasing overpotential the resistance decreases until an overpotential of about 100 mV and remains almost constant until the maximum of 200 mV. Hence, neither a peak nor a strong drop of the resistance is obtained due to the lower maximum DC voltage. The resistance plot shows, that below a certain overpotential, the degradation has a stronger impact on kinetics than the activation with lower voltages.

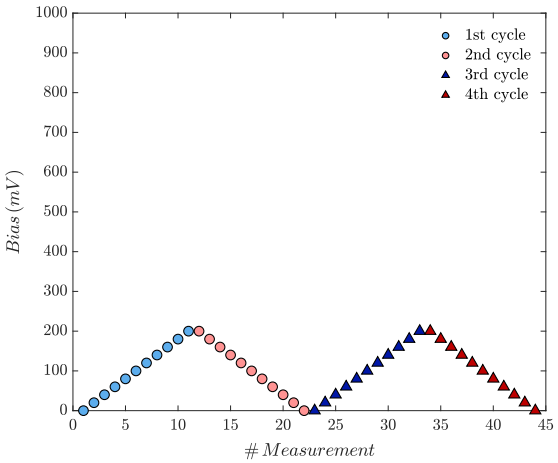

(a) Applied bias over the measurement course

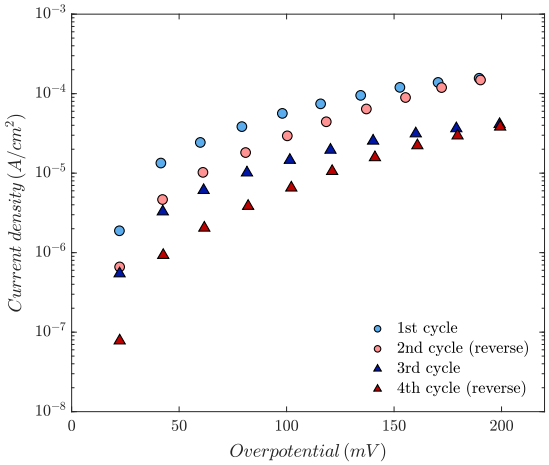

(b) Current-overpotential curve

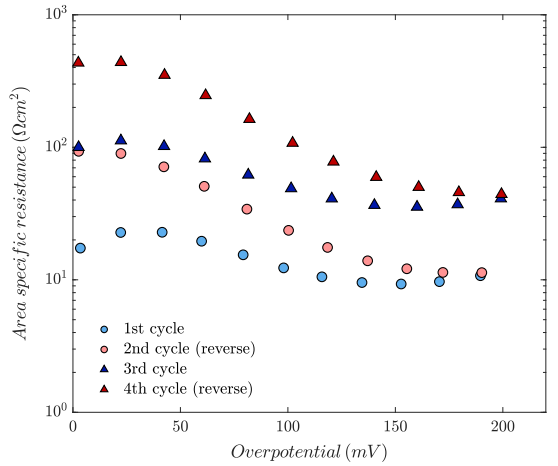

(c) Resistance-overpotential curve

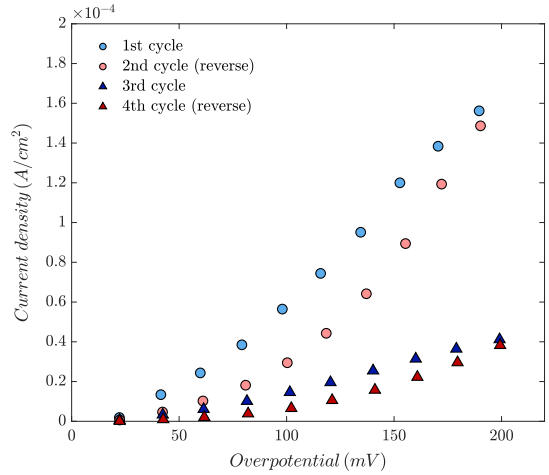

(d) Linear plot of current-overpotential curve

Figure 4.8: Measurements on a pristine microelectrode with a diameter of 195 µm at a measurement temperature of 618 °C; four bias cycles with a maximum DC voltage of 200 mV were applied

Time dependency of the activation

For pristine as well as for degraded electrodes it was shown, that the DC current was higher after a strong activation with DC set voltages up to 1 V, which corresponded to overpotentials of about 385 mV. The time dependency of such activations was investigated by applying a set voltage of 1 V for about 13 min (usual measurement time for one impedance spectrum) and measuring the DC current at a set bias of 200 mV for 20 h after the 1 V pulse, see Figure 4.9 or 4.11. These measurements were performed for pristine electrodes and degraded electrodes with a thermal history.
The applied bias over the measurement course for a pristine electrode can be seen in Figure 4.9. Bias was applied in 50 mV steps from 0 to 250 mV prior the 1 V set bias pulse in order to have a reference before the activation. The 1 V set voltage corresponded to an overpotential of 400 mV. The current-overpotential and the resistance-overpotential plots (Figures 4.10a and 4.10b) reveal that an overpotential of 400 mV for 13 min did not have a strong effect on the current and the resistance measured after this pulse at 200 mV set bias. The Figures 4.10c and 4.10d show the decrease of the current and the increase of the resistance over time of a pristine electrode at a constant set voltage of 200 mV. These results implicate an ongoing degradation and therefore, the Sr segregation to the surface of the electrode at a constant set voltage of 200 mV.

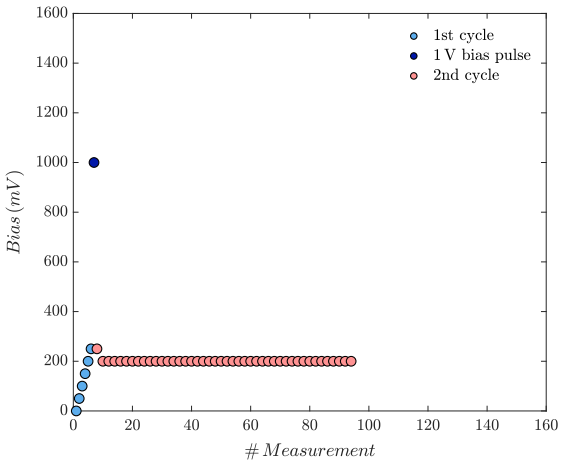

Figure 4.9: Applied bias over the measurement course of a pristine microelectrode

Figure 4.11 shows the applied set bias over the measurement course for a microelectrode, which already had a thermal history of 45.5 h at 612 °C at the beginning of the measurement. The 1 V set bias pulse corresponded to an overpotential of 365 mV. The current-overpotential and resistance overpotential plots (Figures 4.12a and 4.12b) show the strong

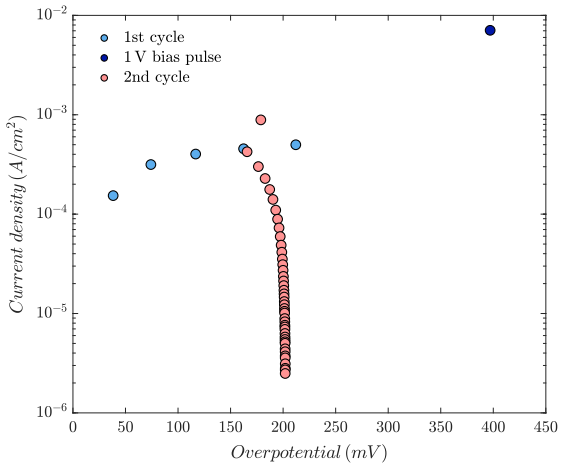

(a) Current-overpotential curve

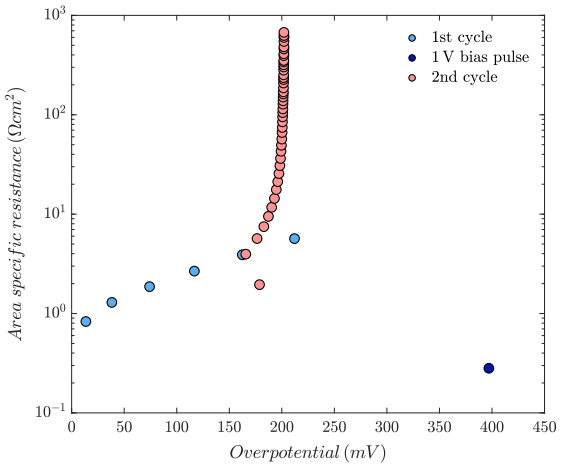

(b) Resistance-overpotential curve

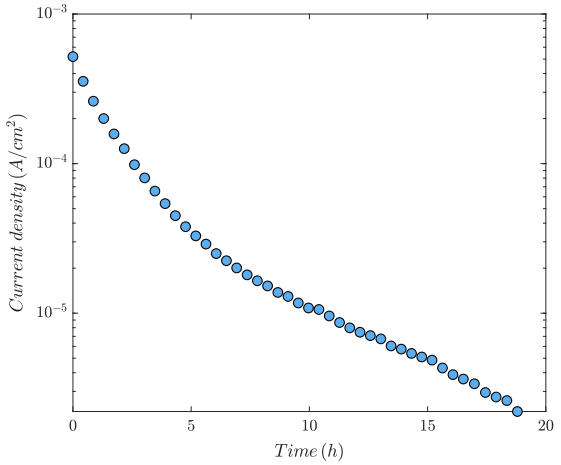

(c) Time dependency of the current at a constant set voltage of 200 mV

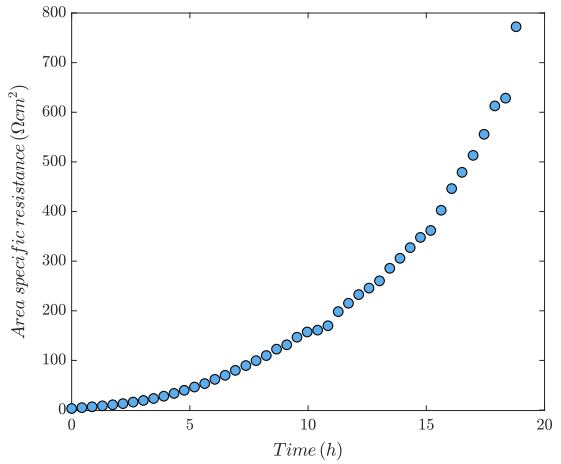

(d) Time dependency of the oxygen exchange resistance at a constant set voltage of 200 mV

Figure 4.10: Measurements on a pristine microelectrode with a diameter of 195 µm at a measurement temperature of 617 °C

activation effect of an overpotential of 365 mV for 13 min. After the bias pulse, the current at 200 mV set bias has increased and the resistance has decreased by one order of magnitude. However, this activation diminished over time due to the ongoing degradation at

200 mV overpotential, which is shown in the Figures 4.12c and 4.12d. After approximately 20 h, both the current and the resistance have almost the same level as they had before the bias pulse.

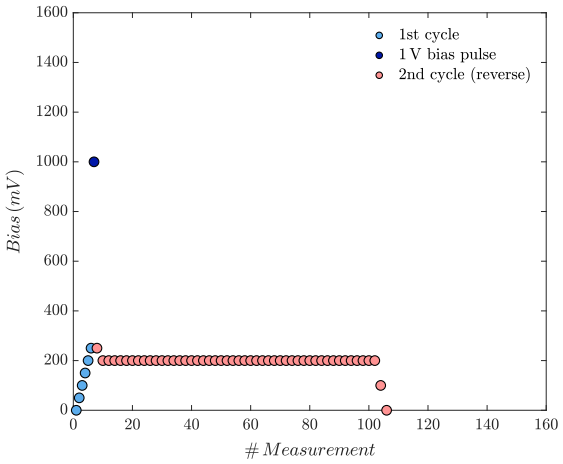

Figure 4.11: Applied bias over the measurement course of a microelectrode with a thermal history of 45.5 h at 612 °C

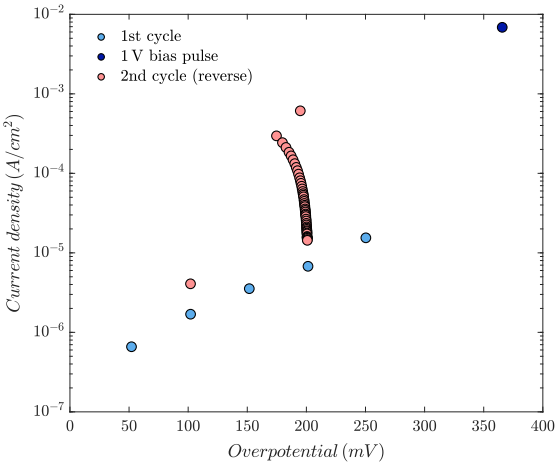

(a) Current-overpotential curve

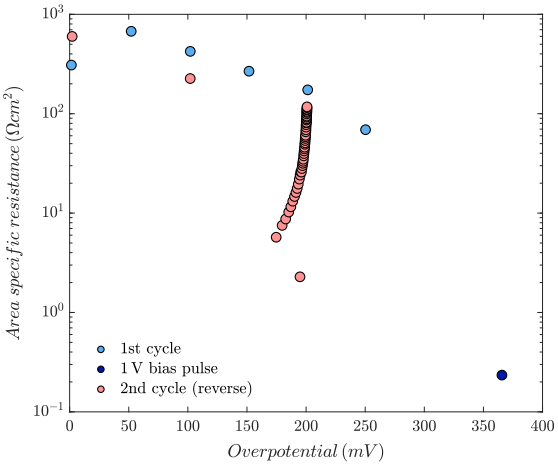

(b) Resistance-overpotential curve

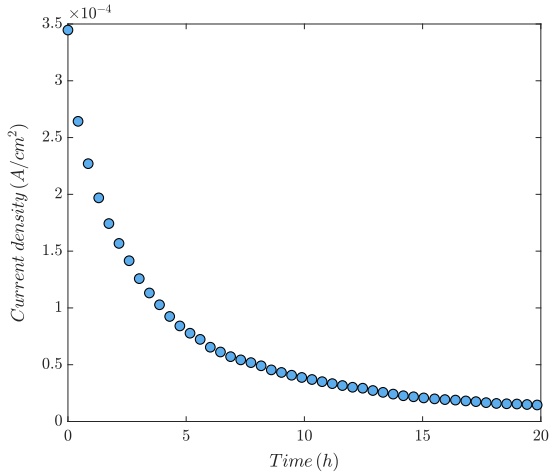

(c) Time dependency of the current at a constant set voltage of 200 mV

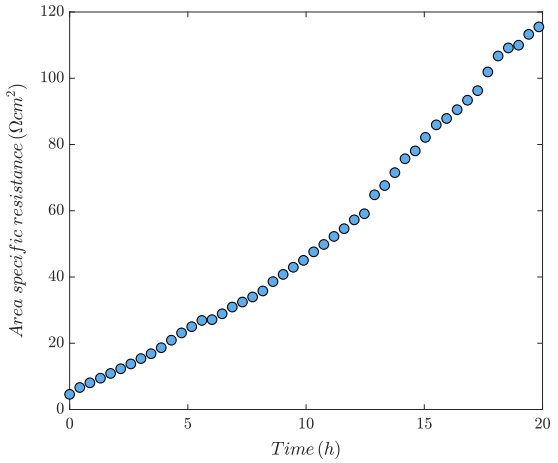

(d) Time dependency of the oxygen exchange resistance at a constant set voltage of 200 mV

Figure 4.12: Measurements on a microelectrode with a diameter of 195 µm and a thermal history of 45.5 h at the measurement temperature of 612 °C

Conclusion

The experiments focusing on the oxygen exchange kinetics revealed a permanent degradation of the LSC microelectrodes. This degradation occurred most likely due to Sr segregation to the surface of the electrodes. However, it was shown that the performance of degraded microelectrodes can be enhanced for a short time by applying high anodic DC voltages corresponding to electrode overpotentials up to 400 mV. In addition, the time dependency of this activation effect was investigated. The reason for this activation remains an open question and more research is definitely needed to understand the underlying mechanisms. Pristine electrodes showed a significant increase of the resistance-overpotential curve in the first bias cycle which led to peaks at overpotentials just below 300 mV. It turned out to be difficult to deconvolute the time dependent degradation and the voltage induced activation during cycling experiments. For example, the peak-like increase of the resistance (i.e. the current plateau) might be partly due to a strong degradation which is then simply reversed at high voltages by the activation effect. Thus, this peak is not visible in reverse cycles after the activation, in cycles containing only lower voltages or in cycles on degraded electrodes.
Similar experiments were done by Baumann et al. [55], who achieved performance improvements of $La_{0.6}Sr_{0.4}Co_{0.8}Fe_{0.2}O_{3-\delta}$ by applying cathodic and anodic DC voltage pulses. They obtained that the magnitude of the activation effect of the anodic bias treatment was smaller than in the case of cathodic bias treatment. Therefore, their focus was on the cathodic bias treatment, which was shown to cause severe changes of the surface composition.

4.2.3 Chemical capacitance

The chemical capacitance was investigated in order to get information about the defect chemistry of LSC microelectrodes upon anodic polarisation. Values of the chemical capacitance were obtained by fitting impedance spectra with equivalent circuits and extracting the relevant parameters. Spectra corresponding to the first group were fitted as explained in section 4.2.1 with one resistance and one R/CPE element. The second group of impedance spectra is characterised by a distinctive linear slope at the high frequency onset of the semicircle, see Figures 4.3a and 4.3b. The equivalent circuit for the second group which was shown in section 4.2.1 with one resistance and two R/CPE elements was used for the determination of the total oxygen exchange resistance. However, a quantitative analysis of the individual features that are present in these spectra turned out to be difficult as the features merge into each other. In order to get the parameters that corresponded to the chemical capacitance of the electrode, an equivalent circuit with a resistance and just one R/CPE element was used. Consequently, the slope feature attributed to a transport

limitation was neglected. Thus, the offset resistance is not only caused by the electrolyte resistance as it was the case before, but also accounts for the transport limitation. However, for the calculations of the overpotential according to equation 2.31 still the high frequency x-axis intercept was used for R_{YSZ}.
For the third-group-spectra according to section 4.2.1 the transport limitation feature becomes more dominant, while the semicircle attributed to the surface exchange resistance and the chemical capacitance gets smaller with increasing bias. In addition, the features merge even more into each other. Therefore, a meaningful fitting with one R/CPE element in order to obtain parameters for the calculation of the chemical capacitance was not possible. As a result, the chemical capacitance was only analysed for overpotentials below approximately 250 mV. The chemical capacitance C_{chem} was calculated as explained in section 2.3.1:

$$C_{chem} = (R_s^{1-n} \cdot Q_{chem})^{\frac{1}{n}} \tag{4.2}$$

Chemical capacitance of pristine electrodes

To investigate the behaviour of the chemical capacitance of pristine electrodes upon anodic polarisation, bias was applied in cycles as shown in Figure 4.13a. DC voltages up to 1000 mV were applied, which corresponded to an electrode overpotential of about 385 mV. However, chemical capacitances could only be analysed for overpotentials up to about 250 mV as explained before. Figure 4.13b shows an example of a measurement with a pristine electrode and it can be seen that the chemical capacitance decreases in the first bias cycle with increasing overpotential. The slope of this decrease is almost linear until an overpotential of about 100 mV. With increasing overpotential higher than 100 mV, the slope of the chemical capacitance curve becomes flatter. As explained in section 2.2, the chemical capacitance reflects the concentration of the minority charge carrier. In synthetic air atmosphere, which was used for all measurements, this minority charge carrier are oxygen vacancies. The concentration of oxygen vacancies is expected to decrease with increasing oxygen partial pressure, which was also shown for $La_{0.6}Sr_{0.4}CoO_{3-\delta}$ by Kawada et al. [56] and for $La_{0.6}Sr_{0.4}Co_{0.8}Fe_{0.2}O_{3-\delta}$ by Baumann et al. [57]. This behaviour is also reflected in the first cycle of the plot in Figure 4.13b, since anodic bias voltage increases the equivalent oxygen partial pressure within the electrode as described in section 2.3.3.
After increasing the DC voltage up to 1000 mV and decreasing it again, the first spectrum from which it was possible to determine the chemical capacitance was measured at an overpotential of about 210 mV and showed a surprisingly high chemical capacitance.

With decreasing bias the chemical capacitance decreases until a minimum around 100 mV was reached. Below 100 mV the chemical capacitance increases again with a similar slope as in the first cycle resulting in an only slightly higher value at open circuit conditions, compared to the very first value. Up to the minimum at 100 mV the chemical capacitance in the third bias cycle is almost the same as in the second cycle. Above 100 mV the chemical capacitance increases again with increasing overpotential which leads to another peak at 210 mV. Then bias is again increased to 1000 mV followed by the fourth cycle with decreasing bias steps. The first meaningful fit of a spectrum determining parameters for the chemical capacitance was once again possible around 210 mV. An even higher peak compared to the previous cycles was obtained. The curve shape of the fourth cycle was similar to those of the second and the third cycle.
As already described, the decrease of the chemical capacitance with increasing overpotential below 100 mV can be explained with the decline of oxygen vacancies. The linear characteristic of this decrease with regard to the logarithmic scale of the chemical capacitance can be explained via the exponential relationship of the equivalent oxygen partial pressure with the overpotential, see equation 2.3.3. This decrease was fitted by using an exponential equation (see equation 4.3) with the parameter A and yielded a slope b of about -0.6 F/RT, see Figure 4.13b.

$$C_{chem} = A \cdot e^{b \cdot \eta_{WE}} \tag{4.3}$$

The corresponding current-overpotential and resistance-overpotential curves to this measurement are shown in Figures 4.5b and 4.5c. Another measurement was performed in which the sample was heated to a temperature of 700 °C for 2 h after the fourth bias cycle. After annealing the sample, two more bias cycles were applied, see Figure 4.14a. The aim of this measurement was to test if the increase of the chemical capacitance could be reversed by exposing the electrode to higher temperatures. As can be seen from Figure 4.14b, annealing at 700 °C does not reverse the increase of the chemical capacitance. Rather, the curves of the fifth and the 6th cycle are similar to those before annealing with the exception of the first cycle. Figures 4.7b and 4.7c show the corresponding current-overpotential and resistance-overpotential curves to this measurement. It was also tried to test the reversibility of the effect by heating samples to temperature of about 800 °C. However, annealing at this temperature led to a drastic change of the impedance spectra, as it is shown in Figure 4.15 for a DC voltage of 120 mV. The newly observed semicircle is most likely attributed to a reaction between lanthanum and / or strontium and zirconium at the electrode / electrolyte interface. Such a reaction at the electrode / electrolyte interface was observed for example by The et al. in terms of $SrZrO_3$ formation between a LSCF electrode and a YSZ electrolyte during SOEC operation [58]. Furthermore, formation of $La_2Zr_2O_7$ was

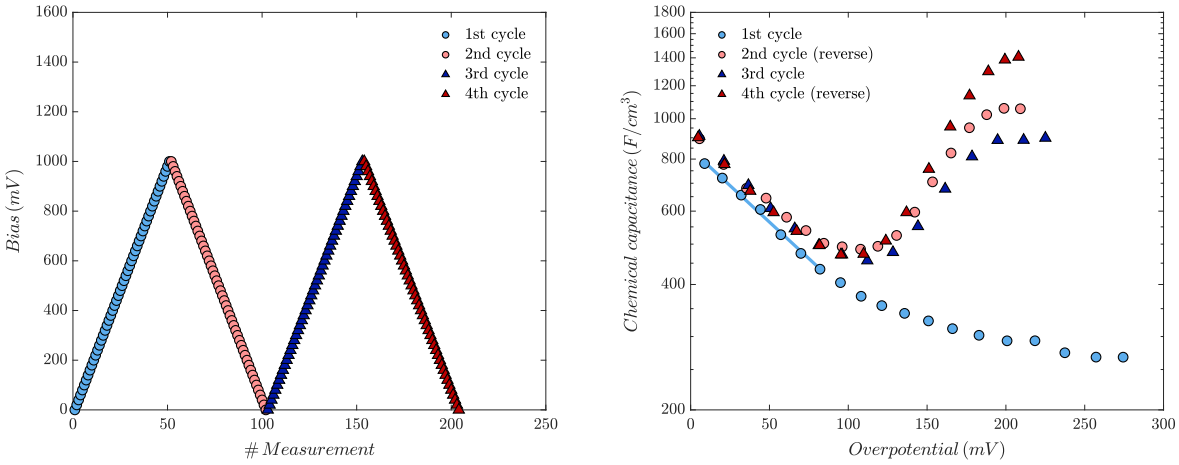

(a) Applied bias over the measurement course (b) Chemical capacitance - overpotential curve

Figure 4.13: Measurements on a pristine microelectrode with a diameter of 195 µm at a measurement temperature of 600 °C

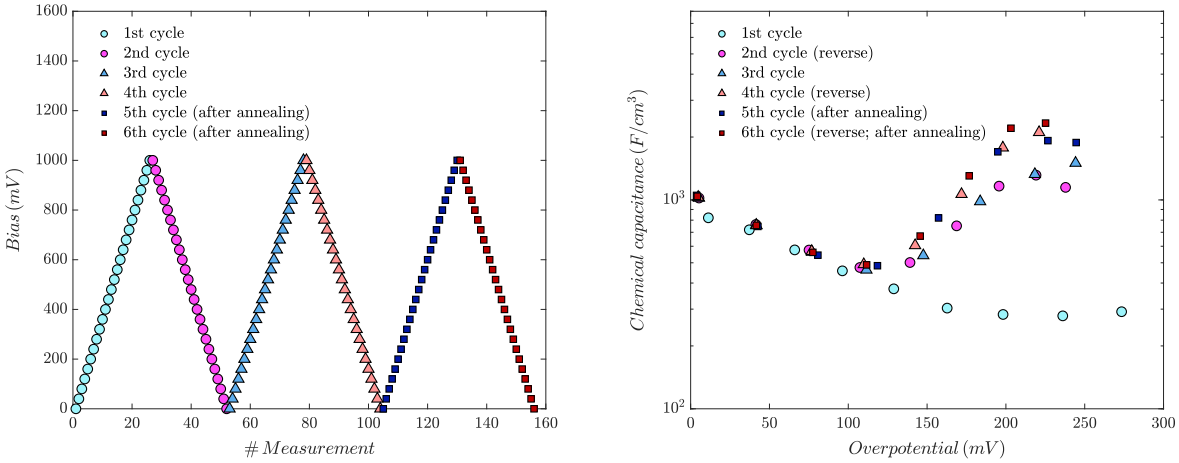

(a) Applied bias over the measurement course (b) Chemical capacitance - overpotential curve

Figure 4.14: Measurements on a pristine microelectrode with a diameter of 195 µm at a measurement temperature of 626 °C; annealing for 2 h at a sample temperature of 700 °C was performed after the fourth bias cycle

frequently reported at higher temperatures [28] [59].

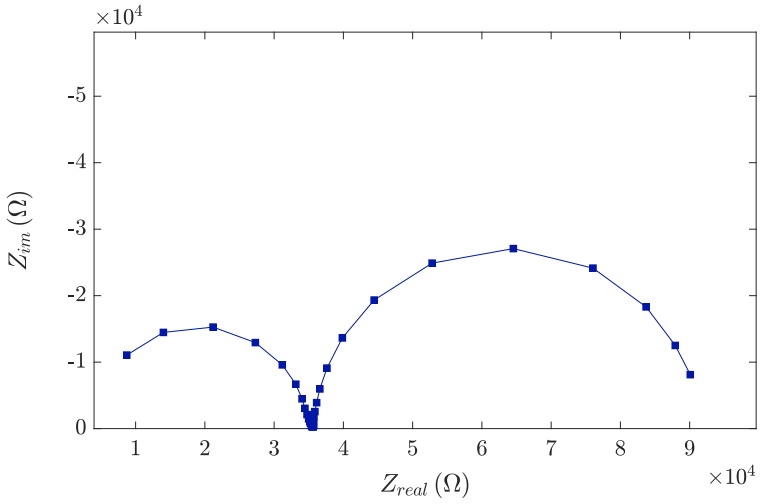

Figure 4.15: Impedance spectrum of a LSC microelectrode with 195 µm diameter and an applied bias voltage of 120 mV after annealing at 800 °C

Chemical capacitance of electrodes with a thermal history

In order to gain more knowledge about the nature of the chemical capacitance peak upon anodic polarisation, measurements were performed with electrodes that already had a thermal history. No voltage has been applied to these electrodes prior the measurement, in order to omit any mechanisms that originate from the anodic overpotential. Bias cycles were applied in the same way as it was shown above for the pristine electrodes, see Figure 4.16a. The plot in Figure 4.16b shows a measurement of a microelectrode with a thermal history of 44 h at 600 °C. Below 100 mV the chemical capacitance decreases as usual with increasing overpotential and the values are very similar for all four cycles. Unlike the measurement with the pristine electrode, the peak of the chemical capacitance around 200 mV appears already in the first cycle. Therefore, it can be concluded, that the mechanism responsible for the increase in chemical capacitance is also triggered without applying high anodic DC voltages. Consequently, this increase may be attributed to degradation mechanisms which occur in synthetic air at the used measurement temperatures. Furthermore, it is shown that the peak value in the second cycle is significantly higher than that of the first cycle. In the third and in the fourth cycle this peak value is again increased. These increases may be attributed to an ongoing degradation of the electrode. The already existent degradation of electrodes with a thermal history is also reflected by the high open circuit resistance of the first bias cycle as it is shown in Figure 4.16d. Figure 4.16c shows the corresponding current-overpotential curve. This measurement was repeated with a sample which had a thermal history of only 6 h at approximately 600 °C, see Figure 4.17a. In Figure 4.17b it can be seen that the behaviour of chemical capacitance is very similar to that of the electrode with a thermal history of 44 h. The corresponding current-overpotential and resistance overpotential curves are shown in Figures 4.6b and 4.6c.

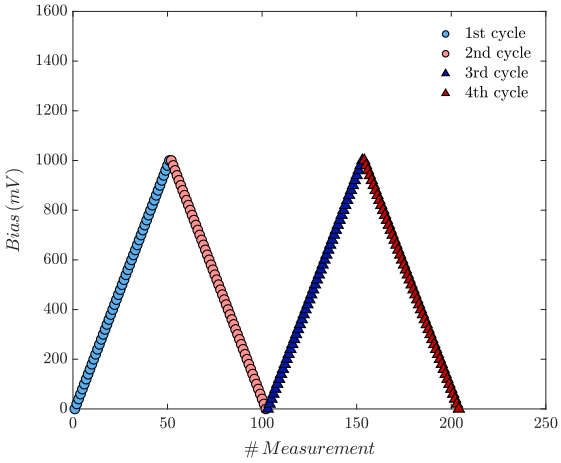

(a) Applied bias over the measurement course

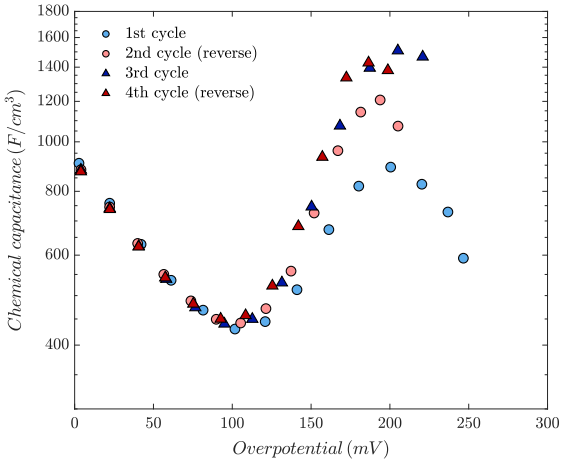

(b) Chemical capacitance - overpotential curve

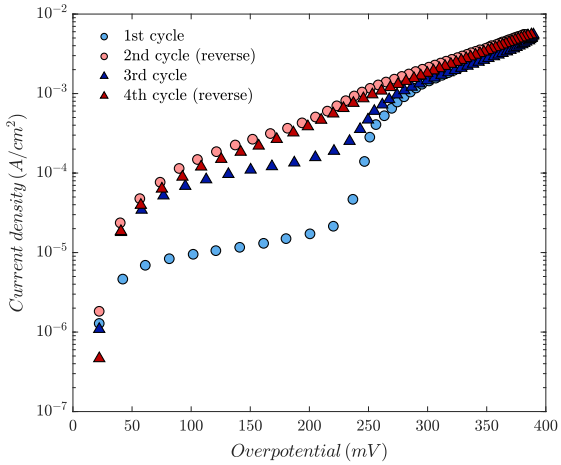

(c) Current-overpotential curve

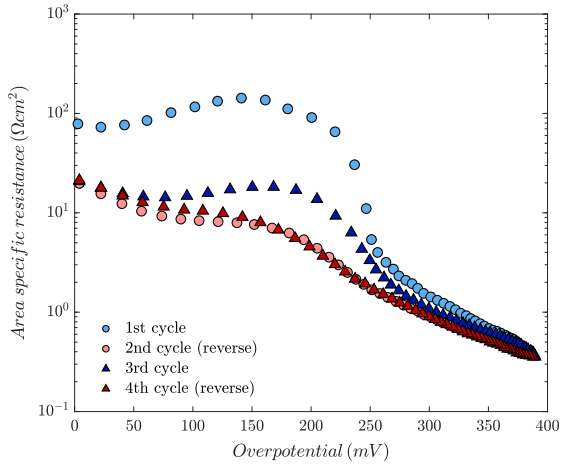

(d) Resistance-overpotential curve

Figure 4.16: Measurements on a microelectrode with a diameter of 195 µm and a thermal history of 44 h at the measurement temperature of 600 °C

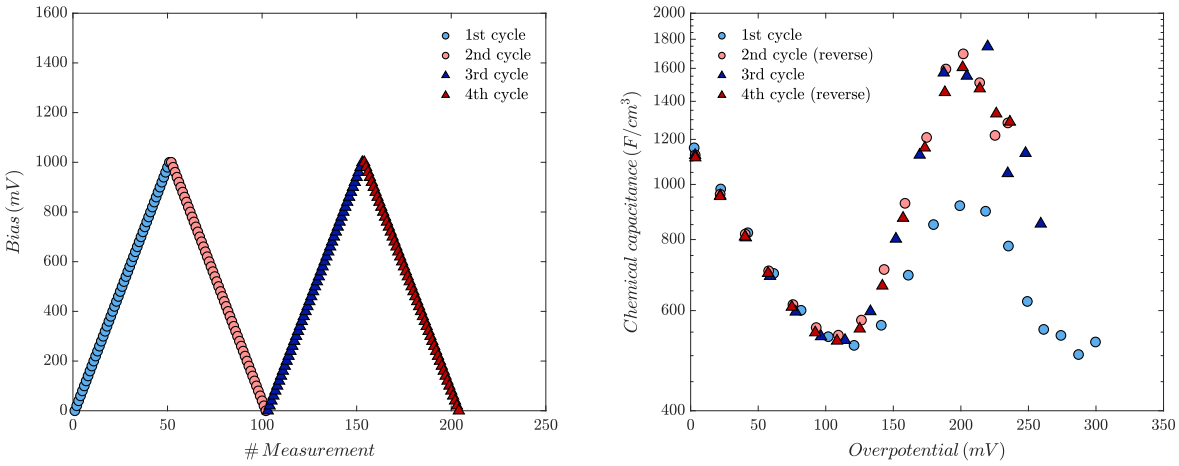

(a) Applied bias over the measurement course (b) Chemical capacitance - overpotential curve

Figure 4.17: Measurements on a microelectrode with a diameter of 195 µm and a thermal history of 6 h at the measurement temperature of 630 °C

Time dependency of chemical capacitance

The experiment described above suggested, that the peak in the chemical capacitance at an overpotential around 200 mV originates from degradation effects that were simply caused by the exposure of the sample to the measurement conditions (synthetic air; 600 °C to 630 °C sample temperature). Hence, the effect of time, in which electrodes were exposed to measurement conditions, was investigated.
At first, experiments were performed with pristine electrodes. Four bias cycles were applied containing maximum DC voltages of 200 mV, which consequently led to a shorter measurement time (Figure 4.18a). Moreover, maximum bias of 200 mV means that it was possible to extract the chemical capacitance from every impedance spectrum. From the chemical capacitance plot in Figure 4.18b it can be seen, that in the first two bias cycles (forward and immediately following backward cycle) the curve behaves like it was shown before in the first cycle of pristine electrodes, which means that there is no peak. By increasing the DC voltage again to 200 mV (at the end of the third and beginning of the fourth cycle), an onset of a peak is visible with a chemical capacitance of about 550 F/cm^3. At that point, the sample was exposed for 7.5 h to the measurement conditions. As a comparison, the first peak of the measurement with a pristine electrode, shown in Figure 4.13b, appeared after a measurement time of 18 h and corresponded to a chemical capacitance of about 1000 F/cm^3. The current-overpotential and resistance-overpotential curves that correspond to the measurement shown in Figure 4.18b can be seen in Figures 4.8b and 4.8c.
For the next experiment, the chemical capacitance of a pristine electrode was measured with bias cycles with maximum DC voltages of 360 mV, see Figure 4.19a. The first bias cycle shows the typical behaviour of the chemical capacitance of pristine electrodes (Figure 4.19b). Then the electrode was exposed to measurement conditions for 20 h without being polarised but still in contact with the platinum needle, which was used for the impedance measurements, see section 3.3.1. After these 20 h another bias cycle was performed, which revealed an increase of the chemical capacitance above 100 mV. The chemical capacitance of a third bias cycle after another 20 h of exposure to measurement conditions, showed a similar behaviour as the second cycle. However, the values of the peak in the chemical capacitance do not exceed 550 F/cm^3, which is quite surprising regarding a measurement time of over 40 h. Here it should be noted, that the above shown measurements of electrodes with thermal history revealed peak values of the chemical capacitance of about 900 F/cm^3 after only 22 h exposure to measurement conditions (Figure 4.17b). This discrepancy may be explained with the cooling effect of the platinum contact needle due to the asymmetric heating of the sample as it was described by Huber and Opitz [60] [51]. Huber et al. showed that for asymmetric heating the contact needle acts as a heat sink and causes lateral temperature gradients. Therefore, it is assumed that the microelectrode, which

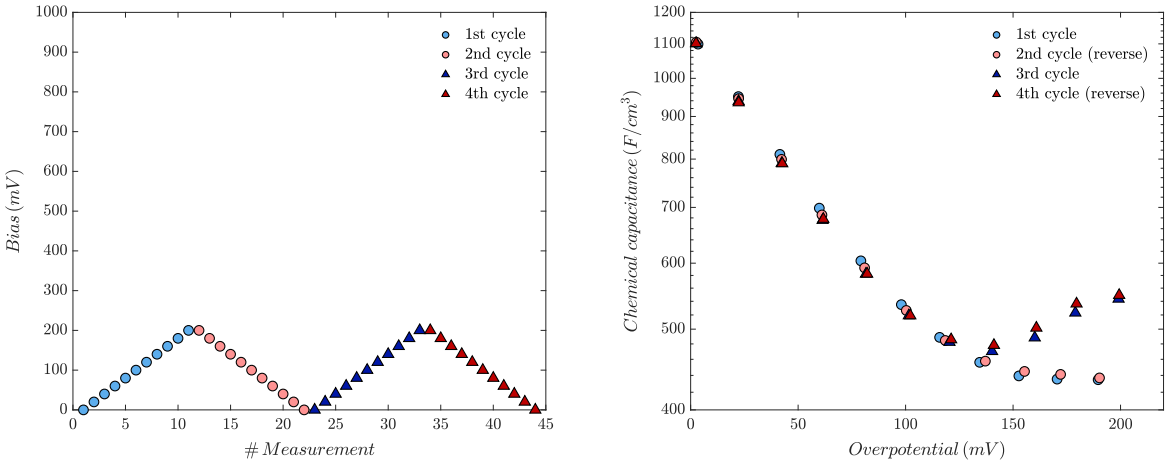

(a) Applied bias over the measurement course (b) Chemical capacitance - overpotential curve

Figure 4.18: Measurements on a pristine microelectrode with a diameter of 195 µm at a measurement temperature of 618 °C; four bias cycles with maximum DC voltages of 200 mV were applied

was contacted during the 40 h of heating at 600 °C (Figure 4.19b) was actually exposed to a lower temperature than the microelectrode with a thermal history of 20 h at 600 °C (Figure 4.17b), which was not contacted during this time. As a consequence, it is supposed that the degradation mechanisms, which are believed to be responsible for the peak in the chemical capacitance, had not been that pronounced in the case of the contacted electrode.

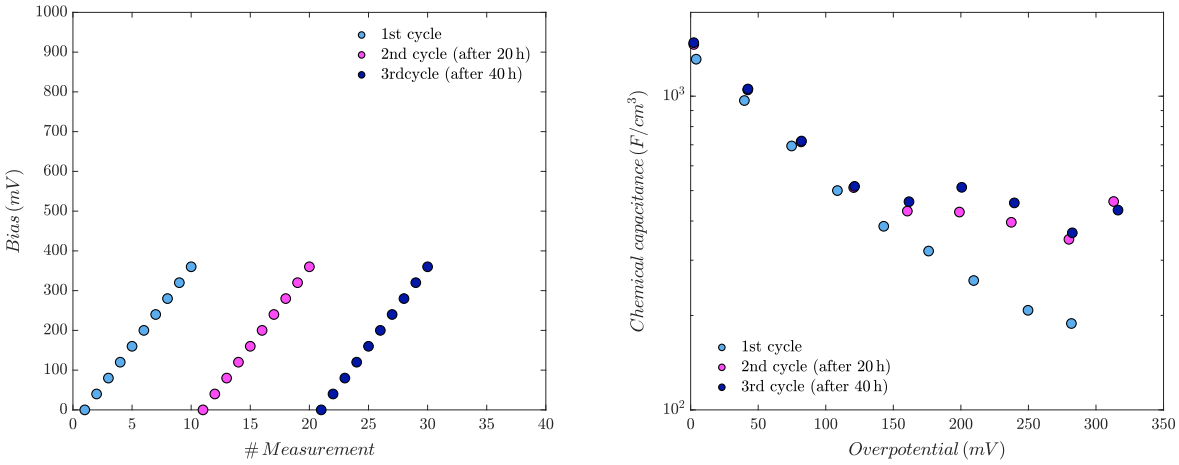

(a) Applied bias over the measurement course (b) Chemical capacitance - overpotential curve

Figure 4.19: Measurements on a pristine microelectrode with a diameter of 195 µm at a measurement temperature of 610 °C

The time dependency of the chemical capacitance of pristine electrodes was also investigated by applying set bias from 0 to 350 mV in 50 mV steps and keeping 350 mV for more than 20 h, see Figure 4.20a. In Figures 4.20b and 4.20d it is shown that the chemical capacitance increases over time at a set bias of 350 mV. However, this increase may be mainly attributed to the increase of the overpotential (Figure 4.20c). The increase of the overpotential over time at a constant set bias can be explained by degradation mechanisms, which were described in section 4.2.2, leading to a decrease of the DC current and thus to a lower voltage drop at the electrolyte. Moreover, the problem regarding the cooling effects of the contact needle was also present for this measurement.
For future experiments, the contact needle has to be removed between measurements or symmetrical heating should be applied for the investigation of the time dependency. However, it will be hardly possible to keep the overpotential at a constant value due to the ongoing degradation of the electrode.

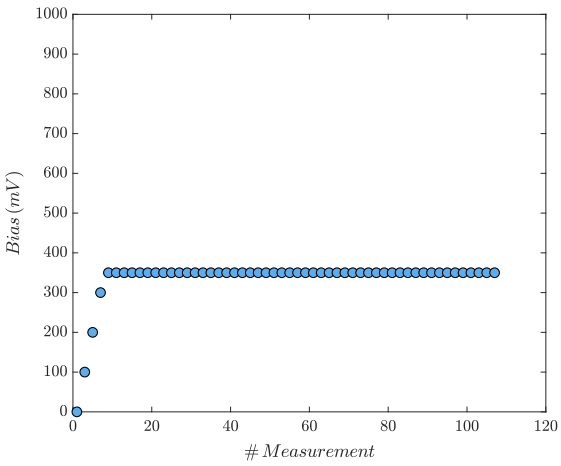

(a) Applied bias over the measurement course

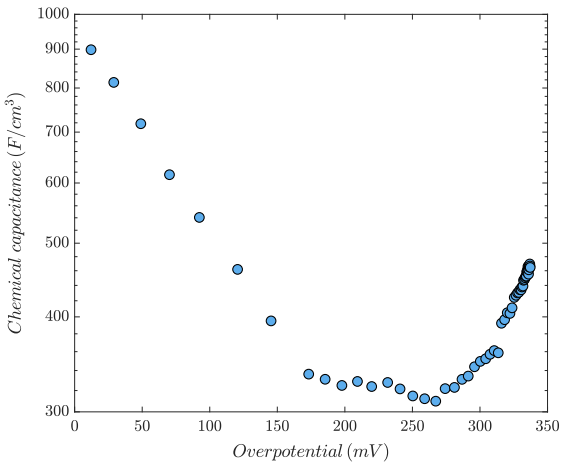

(b) Chemical capacitance - overpotential curve

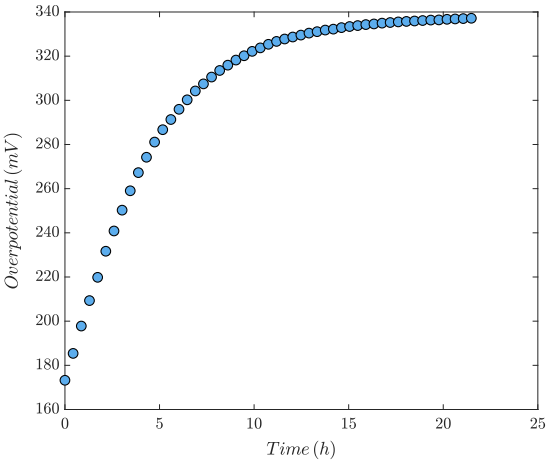

(c) Time dependency of the overpotential at constant set voltage of 350 mV

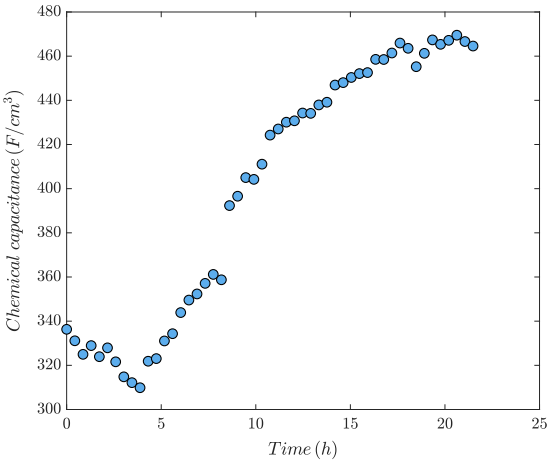

(d) Time dependency of the chemical capacitance at a constant set voltage of 350 mV

Figure 4.20: Measurements on a pristine microelectrode with a diameter of 250 µm at a measurement temperature of 621 °C

Impact of high DC voltages on the chemical capacitance

According to the above mentioned experiments, the peak values of the chemical capacitance were lower if the electrode was contacted during heating. It was shown that even after 40 h of exposing an electrode to a temperature of 600 °C, the peak value upon anodic polarisation did not exceed 550 F/cm^3. Thus, the question remains why pristine samples showed peaks with chemical capacitances of about 1000 F/cm^3 already after 18 h of exposure to measurement conditions, although they were contacted with a platinum needle (Figure 4.13b). The only difference for the latter mentioned measurement was, that DC voltages up to 1000 mV, corresponding to an overpotential of 385 mV, were applied. Therefore, it is suggested that not only degradation due to heating in synthetic air, but also high DC voltages have an impact on the chemical capacitance. As a consequence, measurements were performed with the aim of investigating the effect of high DC voltages.
In the first experiment a pristine electrode was used and DC voltages were applied as shown in Figure 4.21a. The shown decrease of the chemical capacitance with increasing overpotential for pristine electrodes has already been demonstrated by previous measurements. After this first bias cycle, a 1 V set bias pulse, corresponding to an overpotential of 400 mV, was applied. Figure 4.21b reveals, that after this bias pulse the chemical capacitance suddenly increased by more than 100 F/cm^3. These results indicate that high overpotentials have an influence on the chemical capacitance.

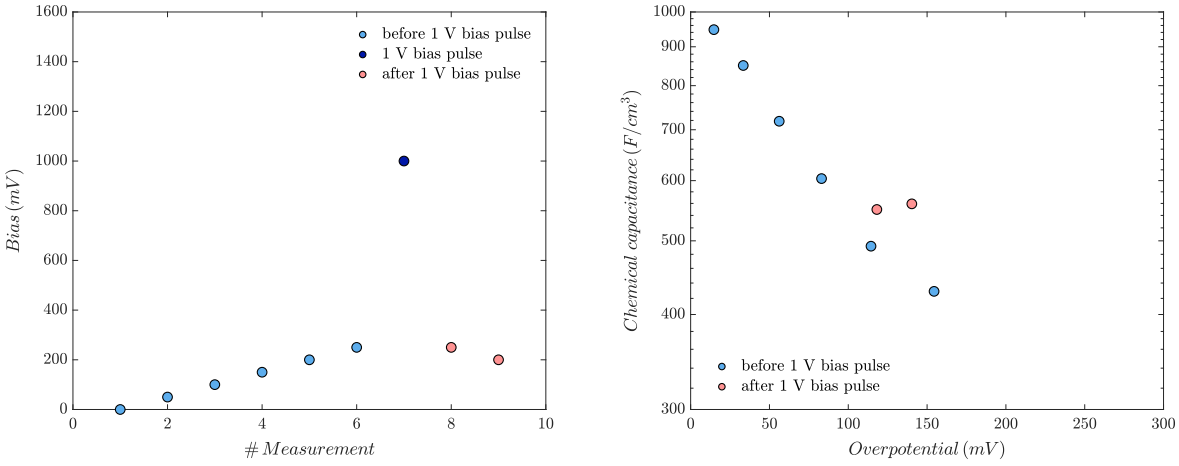

(a) Applied bias over the measurement course (b) Chemical capacitance - overpotential curve

Figure 4.21: Measurements on a pristine microelectrode with a diameter of 195 µm at a measurement temperature of 624 °C

The effect of high DC voltages on the chemical capacitance was also demonstrated by a second experiment with a pristine electrode which is shown in Figure 4.22. For each cycle, a constant bias of 240 mV was applied for 20 h. This bias value corresponds to the typical range for which the peak of the chemical capacitance was observed in previous measurements. At the end of the first and the second cycle, a 1 V set bias pulse (400 mV overpotential) was applied for 13 min. A slight increase from 250 F/cm^3 to 320 F/cm^3 can be observed at the beginning of the first cycle. This increase may be attributed to the increase in overpotential, which is shown in Figure 4.22b. Again an increase in the chemical capacitance due to thermal degradation effects was probably not observed due to the above described cooling effect of the contact needle. However, after the first 1 V bias pulse, a sudden step of more than 100 F/cm^3 appeared. Afterwards, the bias was kept constant again and the chemical capacitance decreased slightly in the beginning of the second cycle, although the overpotential increased at the same time. This behaviour may be attributed to the decrease of the chemical capacitance after the peak around 200 mV overpotential as it can be seen for the first cycles in Figures 4.16b and 4.17b. After the second 1 V bias pulse, there is again a sudden increase of more than 100 F/cm^3. Then again a slight decrease of the chemical capacitance can be observed at the beginning of the third cycle. From these measurements it can be concluded that high overpotentials of around 400 mV have a strong impact on the chemical capacitance. Hence, the high peaks of the chemical capacitance of pristine electrodes, that occurred already after 18 h of heating while being permanently contacted, can be explained by the application of high DC voltages. Due to the previously described experiments using electrodes with a thermal history, it was concluded that the mechanism responsible for the increase of the chemical capacitance is linked to the degradation of the electrodes. Therefore, it seems that high anodic voltages also lead to degradation of the electrodes.

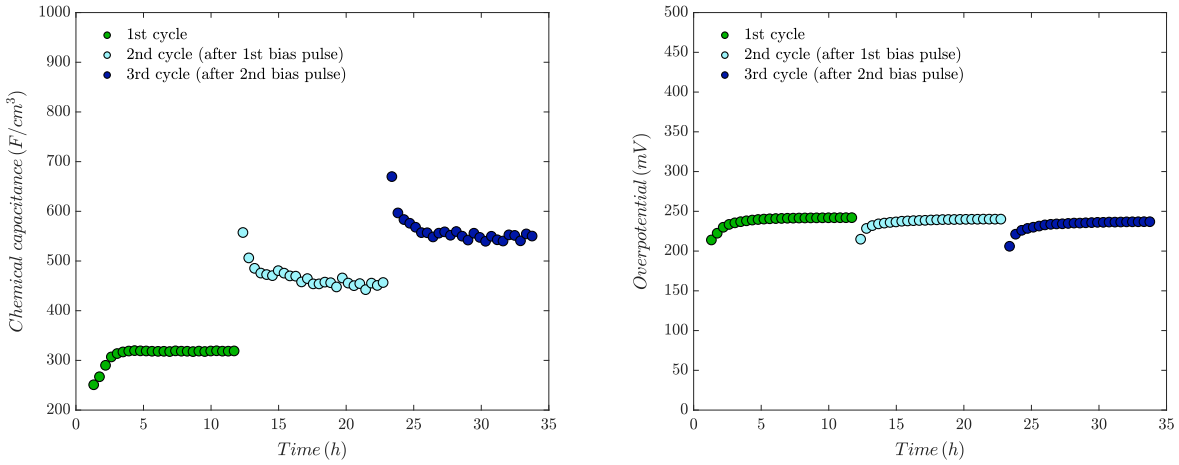

(a) Time dependency of the chemical capacitance at a constant set voltage of 240 mV

(b) Time dependency of the overpotential at a constant set voltage of 240 mV

Figure 4.22: Measurements on a pristine microelectrode with a diameter of 195 µm at a measurement temperature of 612 °C with two bias pulses (1 V set, about 400 mV overpotential, for 13 min)

Conclusion

The performed experiments showed a decrease of the chemical capacitance with increasing anodic overpotential below 100 mV. Since the chemical capacitance reflects the minority charge carrier concentration, this decrease was expected due to the decline of oxygen vacancies with increasing anodic overpotential. Although with a smaller slope, the chemical capacitance of pristine electrodes continued to decrease even at higher overpotentials than 100 mV. However, after heating the electrodes for several hours at around 600 °C or after applying high bias voltages up to 1 V, a peak of the chemical capacitance was observed at overpotentials higher than 100 mV. This peak of the chemical capacitance is not reversible by heating the samples to approximately 700 °C. To the best of the authors' knowledge, this increase of the chemical capacitance upon anodic polarisation has not been reported yet in literature.
The author suggests that degradation mechanisms are responsible for the increase of the chemical capacitance upon anodic polarisation. As already mentioned, Kubicek et al. [54] showed that annealing at 600 °C leads to degradation of LSC electrodes in terms of Sr segregation to their surfaces. Furthermore, they showed that this Sr segregation to the surface leads to an increase of the oxygen exchange resistance. This increase of the oxygen exchange resistance was also observed in this work. Hence, it is concluded that Sr segregation occurred also for the electrodes which were used within this study. Assuming Sr segregating to the surface implicates the formation of A site vacancies, V_A''', in the bulk of LSC. Moreover, a peak in the chemical capacitance indicates a change of the minority charge carrier concentration. As already described, oxygen vacancies are believed to decrease with increasing anodic overpotential. Therefore, an increase of the chemical capacitance at higher anodic overpotential suggests involvement of an additional point defect species. One possible hypothesis is that these point defects are A site vacancies, which were formed over time at around 600 °C. What is more, it was shown that high overpotentials of about 400 mV further increase the chemical capacitance. According to our suggested hypothesis of A site vacancies as decisive defects, this indicates an accelerated formation of Sr vacancies at high anodic voltages (Please note: this is the voltage regime where the oxygen exchange kinetics were activated).
However, since the chemical capacitance is determined by $\partial\mu_O/\partial c_O$ (see equation 2.11), the suggested formation of A site vacancies has to somehow influence the chemical potential of oxygen and the oxygen content. It is supposed that peroxide ions O_2^{2-} are formed with increasing anodic overpotential. Such a formation of peroxo-like species was also shown by McCalla et al. [61] for anionic redox reactions in Li-rich layered oxides. These peroxide ions may be formed close to A site vacancies. In equation 4.4a the usual oxygen exchange reaction is shown. The proposed reaction of A site vacancies with oxygen to form peroxide ions is formally described by equation 4.4b.

$$\frac{1}{2}\,\mathrm{O}_\mathrm{O}^\times + \mathrm{V}_\mathrm{O}^{\bullet\bullet} + 2\,\mathrm{Co}_\mathrm{Co}^\times \rightleftharpoons \mathrm{O}_\mathrm{O}^\times + 2\,\mathrm{h}(\mathrm{Co}_\mathrm{Co}^\bullet) \tag{4.4a}$$

$$\frac{1}{2}\,\mathrm{O}_2 + \mathrm{V}_\mathrm{A}''' + \mathrm{O}_\mathrm{O}^\times \rightleftharpoons (\mathrm{O}_\mathrm{A}''''\text{–}\mathrm{O}_\mathrm{O}^\bullet) \tag{4.4b}$$

Alternatively one may write

$$\frac{1}{2}\,\mathrm{O}_2 + \mathrm{V}_\mathrm{A}''' + \mathrm{O}_\mathrm{O}^\times \rightleftharpoons (\mathrm{V}_\mathrm{A}'''\text{–}(\mathrm{O}_2)_\mathrm{O}^\times) \tag{4.5}$$

in order to emphasise that the peroxo-species is somewhere between an oxide ion site and the A site.
Assuming the above explained mechanism, it is also possible to determine the Sr deficiency in the bulk of LSC with the help of the amount of charge that corresponds to the peak of the chemical capacitance. This charge can be calculated by the integration of the chemical capacitance C_{chem} over the overpotential of the working electrode η_{WE}. In order to understand why the charge can be calculated via this integration, a few definitions are needed. Equation 4.6a shows the definition of the volume specific chemical capacitance C_{chem} with the elementary charge e instead of the Faraday constant. The chemical potential of oxygen μ_O depends on the oxygen partial pressure p_{O_2} and the overpotential of the working electrode η_{WE}, see equation 4.6b. Here, the oxygen chemical potential is related to 1 bar oxygen. Equation 4.6c describes the definition of the oxygen concentration inside the material via the absolute values of the total charges per cm^3 of the two different oxygen ion species, $Q_{O^{2-}}$ and $Q_{O_2^{2-}}$. The oxygen site concentration is expressed by n^0.

$$\frac{C_{chem}}{V} = 4e^2 n^0 \cdot \left(\frac{\partial \mu_O}{\partial c_O}\right)^{-1} \tag{4.6a}$$

$$\mu_O = \mu_O^0 + \frac{kT}{2} \cdot ln\left(\frac{p_{O_2}}{1\,bar}\right) + 2e\eta_{WE} \tag{4.6b}$$

$$c_O = \frac{Q_{O^{2-}}}{2e \cdot n^0} + \frac{Q_{O_2^{2-}}}{2e \cdot n^0} \tag{4.6c}$$

Inserting equation 4.6b in equation 4.6a and using the definition of equation 4.6c reveals how the chemical capacitance is linked to the charge:

$$\frac{C_{chem}}{V} = 4e^2n^0 \cdot \left(\frac{\partial \mu_O}{\partial c_O}\right)^{-1} = 4e^2n^0 \cdot \left(\frac{\partial \mu_O^0}{\partial c_O} + \frac{\partial\left(\frac{kT}{2} \cdot ln\left(\frac{p_{O_2}}{1\,bar}\right)\right)}{\partial c_O} + \frac{\partial(2e\eta_{WE})}{\partial c_O}\right)^{-1}$$
$$= 4e^2n^0 \cdot \left(\frac{\partial(4e^2n^0 \cdot \eta_{WE})}{\partial Q_{O^{2-}} + \partial Q_{O_2^{2-}}}\right)^{-1} \tag{4.7a}$$

$$\frac{C_{chem}}{V} = \frac{\partial Q_{O^{2-}}}{\partial \eta_{WE}} + \frac{\partial Q_{O_2^{2-}}}{\partial \eta_{WE}} \Rightarrow Q_{O_2^{2-}} = \int_{peak} \frac{C_{chem,O_2^{2-}}}{V}\, d\eta_{WE} - \int_{peak} \frac{C_{chem,O^{2-}}}{V}\, d\eta_{WE} \tag{4.7b}$$

In order to obtain the charge $Q_{O_2^{2-}}$ that corresponds to the chemical capacitance increase $C_{chem,O_2^{2-}}$ which is attributed to the new oxygen species, it is necessary to subtract the chemical capacitance $C_{chem,O^{2-}}$ caused by the oxygen vacancy concentration change. This is approximated by the subtraction of the minimum value at around 100 mV, $C_{chem,min}$:

$$Q_{O_2^{2-}} \approx \int_{peak} \frac{C_{chem,O_2^{2-}} - C_{chem,min}}{V}\, d\eta_{WE} \tag{4.8}$$

For the calculation of the A site deficiency per unit cell, the elementary charge e, the total charge of the peak $Q_{O_2^{2-}}$ and the number of unit cells per cm^3, γ, is needed. The latter is calculated via the lattice constant a of LSC. From a crystal structure data base a lattice constant for cubic $La_{0.6}Sr_{0.4}CoO_{3-\delta}$ (Ref. ICSD 01-080-6496) of 3.8394 Å was used:

$$\gamma = \frac{10^{-6}}{a^3} \approx 1.7669 \cdot 10^{22}\,(unit\ cells\ /\ cm^3) \tag{4.9}$$

Hence, the A site deficiency per unit cell, χ, is calculated as follows:

$$\chi = \frac{Q_{O_2^{2-}}}{\gamma \cdot e} \tag{4.10}$$

The A site deficiency per unit cell χ was exemplary calculated for a measurement in which an electrode with a thermal history of 44 h at 600 °C has been used. $Q_{O_2^{2-}}$ has been calculated by integrating the chemical capacitance from the onset of peak to the highest value of the peak and multiplying this value by two, assuming a symmetric shape of the peak. As already explained, the chemical capacitance values have to be reduced by the minimum values in order to account for the charge which is attributed to the peroxo species. The resulting area which corresponds to the charge $Q_{O_2^{2-}}$ is shown in Figure 4.23.

Table 4.1 shows the calculated values for the total charges of oxygen per cm^3, $Q_{O_2^{2-}}$, and

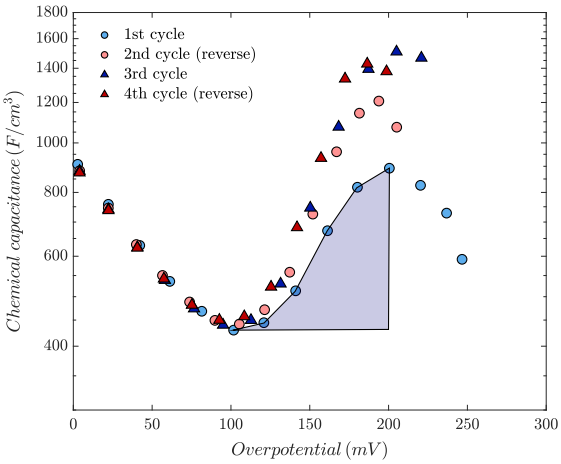

Figure 4.23: Chemical capacitance of a microelectrode with a diameter of 195 µm and a thermal history of 44 h at 600 °C

the corresponding A site deficiencies, χ, for each peak of the measurement shown in Figure 4.23.

Table 4.1: Strontium deficiency of LSC calculated via peaks of the chemical capacitance

Peak	$Q_{O_2^{2-}}$ (C/cm^3)	χ
1st bias cycle	38.0915	0.0135
2nd bias cycle	56.5202	0.0200
3rd bias cycle	92.4843	0.0327
4th bias cycle	64.5052	0.0228

The above described calculations indicate that peaks of the chemical capacitance upon anodic polarisation could serve as a measure for A site deficiency in the bulk of an electrode. This would allow a quantitative estimation of the strontium segregation to the surface and therefore, the degradation of an electrode.

4.3 Scanning electron microscopy

The surface morphology of microelectrodes was investigated via scanning electron microscopy (SEM). SEM images have been recorded of pristine as well as of electrodes with various thermal and polarisation histories, see Figures 4.24a - 4.24c. No correlations between electrode histories and morphologies were noticeable. However, grains with a size of 50-100 nm were observed on the surfaces of all microelectrodes, even on the pristine ones, see Figure 4.24c. Furthermore, cracks were found on all surfaces. These cracks were most likely formed during the cooling to room temperature after the pulsed laser deposition due to different thermal expansion coefficients between LSC and the YSZ substrate.

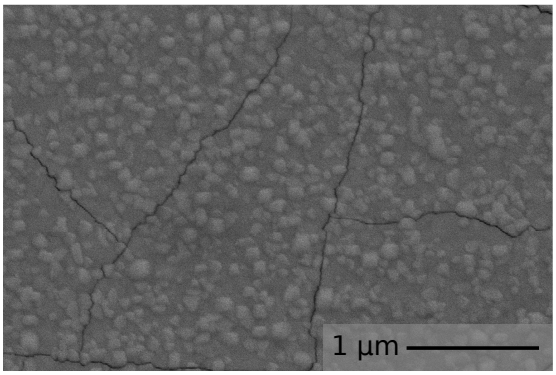

(a) Pristine electrode

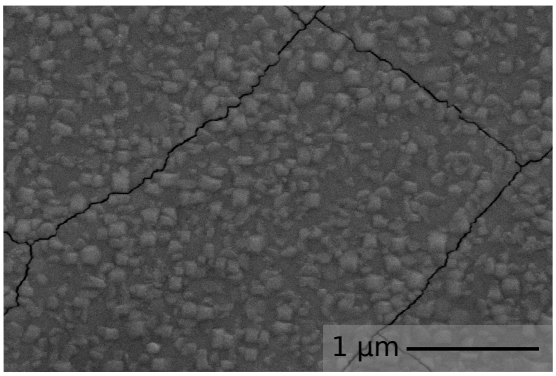

(b) Electrode with thermal history

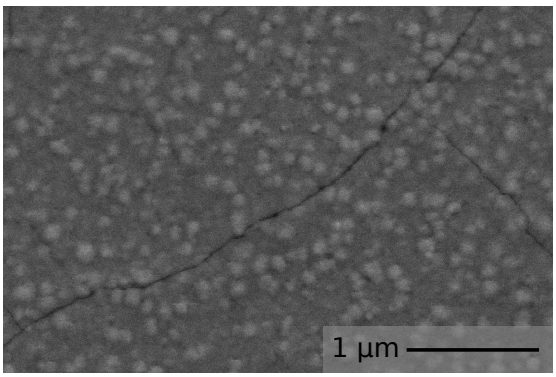

(c) Electrode with thermal and polarisation history

Figure 4.24: SEM images of LSC thin film microelectrodes

4.4 X-ray diffraction

The structural composition of the LSC thin film microelectrodes was investigated by means of X-ray diffraction (XRD). Figure 4.25 shows diffraction patterns of an annealed electrode which was "frozen" at around 250 mV overpotential and an annealed electrode without polarisation history. In this context "frozen" means that the sample was taken out of the measurement chamber during a measurement at 250 mV and was rapidly cooled to room temperature. An overpotential of about 250 mV lies within the overpotential range where the increase of the chemical capacitance was observed, see section 4.2.3. As can be seen, no significant differences were observed between the XRD patterns of annealed electrodes without polarisation history and electrodes that were "frozen" at around 250 mV.
By comparison with a XRD-database, all peaks could be assigned to $La_{0.6}Sr_{0.4}CoO_{3-\delta}$ or to the YSZ substrate. Since the thin LSC film grew relative to the [100] YSZ plane, the diffraction pattern reveals intense [200] and [400] peaks of the YSZ substrate. Moreover, it can be observed that the thin LSC film grew preferentially in [100] and [110] direction. The low intensity of the peaks is due to the 0.3 mm slit which was used in order to focus the beam on individual microelectrodes.

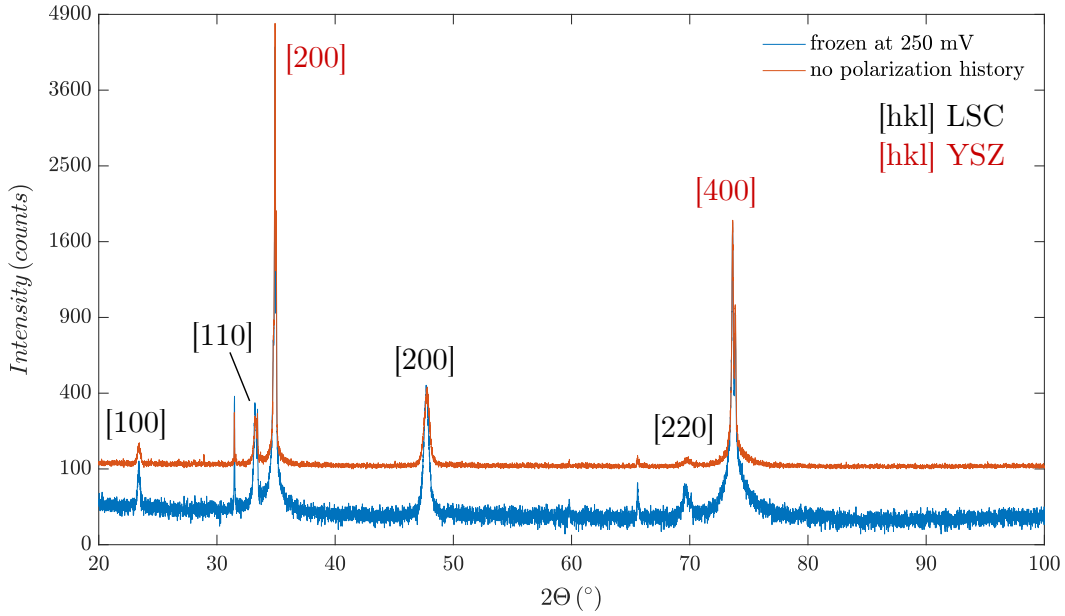

Figure 4.25: XRD pattern of an LSC thin film microelectrode deposited on a YSZ substrate

5 Summary

LSC thin films were deposited on YSZ single crystals via pulsed laser deposition. Microstructuring of the thin films was done with photolithography and ion beam etching to obtain microelectrodes with a diameter of 195 - 300 µm. Porous LSC was used for the counter electrodes, which was deposited on the back side of the samples.
The electrochemical behaviour of the thin film microelectrodes upon anodic polarisation was analysed by impedance spectroscopy. The obtained impedance spectra were fitted with suitable equivalent circuits. Oxygen exchange kinetics and defect chemistry were analysed by extracting the corresponding fit parameters. Measurements were done in synthetic air with different anodic polarisations and sample temperatures between 600 °C and 630 °C.
The LSC microelectrodes showed a permanent degradation in terms of an increasing oxygen exchange resistance over time. This degradation was most likely caused by strontium segregation to the surface as it was shown in previous studies. However, it was observed that the performance of the electrodes can be improved for a short time by applying high anodic DC voltages. This activation effect diminished over time due to the ongoing degradation. The reason for this activation remains an open question and more research is needed to understand the underlying mechanisms.
The defect chemistry of the LSC electrodes was investigated by analysing the chemical capacitance. Below 100 mV the chemical capacitance decreased with increasing anodic overpotential. This decrease can be attributed to the decline of oxygen vacancies, which are expected to be the minority charge carriers in synthetic air. After heating the electrodes for several hours at around 600 °C or after applying high bias up to 1 V, a peak of the chemical capacitance was obtained for overpotentials higher than 100 mV. This peak of the chemical capacitance was not reversible by heating the samples to approximately 700 °C. It is supposed that degradation and therefore strontium segregation to the surface is responsible for this increase of the chemical capacitance upon anodic polarisation. Assuming strontium segregation to the surface implicates the formation of A site vacancies in the bulk of the electrodes. A mechanism that connects the oxygen exchange reaction and A site vacancies was proposed. It is suggested that peroxide ions O_2^{2-} are formed upon anodic DC voltages. These peroxide ions may occupy A site vacancies resulting in consumption of electrons. Assuming this mechanism, the strontium deficiency of a microelectrode was determined via the amount of charge that corresponds to the peak of the chemical capacitance. This charge was calculated via the integration of the volume specific

capacitance over the overpotential of the microelectrode. Strontium deficiency values in the range of 1-3 % with respect to lattice sites were found. As a consequence, it is suggested that the chemical capacitance upon anodic polarisation could serve as a measure for strontium segregation to the surface and thus for the degradation of an electrode.

Danksagung

Ich kann es noch gar nicht wirklich fassen, dass ich hier die letzten Zeilen meiner Diplomarbeit verfasse. Nach sehr spannenden, aufschlussreichen, lustigen und manchmal auch stressigen elf Monaten befinde ich mich nun also in der finalen Phase der Diplomarbeit. Damit naht auch das Ende meiner Studienzeit. Um ehrlich zu sein, fühlt sich das surreal an, kommt es mir doch manchmal so vor, als wäre es gestern gewesen, dass ich in meiner ersten Physik-Vorlesung im völlig überfüllten Hörsaal auf den Stiegen saß. Dieses Kapitel ist all jenen gewidmet, die mich auf dem Weg vom Studienbeginn bis hin zur Fertigstellung meiner Diplomarbeit unterstützt haben.

Als Erstes möchte ich mich bei Prof. Jürgen Fleig bedanken, der mir nicht nur diese Diplomarbeit in seiner Arbeitsgruppe ermöglichte, sondern sich auch immer Zeit für meine Fragen und für fachliche Diskussionen nahm.

Ein großer Dank gebührt auch meinem Betreuer Alexander Schmid, der mich in die Welt der Festkörperelektrochemie eingeführt hat und ohne dessen laufende Unterstützung bei allen möglichen aufgetretenen Problemen es meine Diplomarbeit in dieser Form nicht gäbe. Weiters möchte ich meinem Bürokollegen Harald Summerer für den IT-Support und die gemeinsamen Raunzereien über an manchen Tagen unüberwindbar wirkende Probleme danken.

Ein großes Dankeschön gilt auch Matthäus Siebenhofer für die Unterstützung bei den XRD-Messungen und für die Betreuung meiner Projektarbeit, deren Ergebnisse der Ausgangspunkt für diese Diplomarbeit war. Außerdem hat er gemeinsam mit Alexander Viernstein einen großen Anteil dazu beigetragen, dass ich mich in der Arbeitsgruppe von Anfang an aufgenommen und sehr wohl gefühlt habe – dafür bin ich euch sehr dankbar!

Darüber hinaus möchte ich mich bei der gesamten Elektrochemie-Arbeitsgruppe für das hervorragende Arbeitsklima bedanken, welches dafür sorgt, dass auch in schwierigen Zeiten der Spaß beim wissenschaftlichen Arbeiten nicht zu kurz kommt.

Wie bereits erwähnt, bedeutet das Ende meiner Diplomarbeit auch den baldigen Abschluss meiner Studienzeit. Daher möchte ich diese Gelegenheit nutzen und mich bei meiner Lerngruppe bedanken – ohne euch wäre das Studium nicht nur um ein Vielfaches schwieriger, sondern auch nur halb so lustig gewesen! Insbesondere danke ich dir, Anna, für unser gemeinsames Lernen und Rechnen für fast alle Prüfungen und Übungen im Bachelor. Es freut mich sehr, dass dabei und beim gemeinsamen Verfolgen von einigen sportlichen Veranstaltungen eine wunderbare Freundschaft entstanden ist. Außerdem möchte ich hier

Johanna, Manuel, Daniel und Gabriel erwähnen – auch ihr habt meine Studienzeit zu einer ganz besonderen gemacht.
Des Weiteren möchte ich mich bei all meinen Freunden für die oft notwenige Ablenkung und die mentale Unterstützung in schwierigen Zeiten bedanken. Besonders dir, Felix, danke ich dafür, dass ich mit dir stets über alles sprechen kann und es bei den gemeinsamen Abendessen immer etwas zu lachen gibt.
Auch dir, Claudia, möchte ich ein riesengroßes Dankeschön für deine Unterstützung in den letzten drei Jahren aussprechen. Danke, dass du an meiner Seite bist und du dir immer alle meine Probleme anhörst!
Der größte Dank gebührt meiner Familie, insbesondere meinen Eltern, Margit und Erwin, die mir dieses Studium ermöglicht haben und meinem Bruder Stefan – es ist unbeschreiblich wertvoll für mich, so jemanden wie dich an meiner Seite zu haben! Danke, dass ihr immer für mich da seid und mich stets unterstützt!

List of Figures

Bibliography

[1] I. E. Agency. *World Energy Balances*. October 2019. URL: https://www.iea.org/statistics/balances/.

[2] I. E. Agency. *Climate change*. October 2019. URL: https://www.iea.org/topics/climatechange/.

[3] I. E. Agency. *Hydrogen. A key part of a clean and secure energy future*. October 2019. URL: https://www.iea.org/topics/hydrogen/production/.

[4] A. Buttler and H. Spliethoff. "Current status of water electrolysis for energy storage, grid balancing and sector coupling via power-to-gas and power-to-liquids: A review". In: *Renewable and Sustainable Energy Reviews* 82 (Feb. 2018), pp. 2440–2454. DOI: 10.1016/j.rser.2017.09.003.

[5] P. Moçoteguy and A. Brisse. "A review and comprehensive analysis of degradation mechanisms of solid oxide electrolysis cells". In: *International Journal of Hydrogen Energy* 38.36 (Dec. 2013), pp. 15887–15902. DOI: 10.1016/j.ijhydene.2013.09.045.

[6] W. Doenitz, R. Schmidberger, E. Steinheil, and R. Streicher. "Hydrogen production by high temperature electrolysis of water vapour". In: *International Journal of Hydrogen Energy* 5.1 (1980), pp. 55–63. DOI: 10.1016/0360-3199(80)90114-7.

[7] K. Chen and S. P. Jiang. "Review - Materials Degradation of Solid Oxide Electrolysis Cells". In: *Journal of The Electrochemical Society* 163.11 (2016), F3070–F3083. DOI: 10.1149/2.0101611jes.

[8] A. Hauch, S. D. Ebbesen, S. H. Jensen, and M. Mogensen. "Solid Oxide Electrolysis Cells: Microstructure and Degradation of the Ni/Yttria-Stabilized Zirconia Electrode". In: *Journal of The Electrochemical Society* 155.11 (2008), B1184. DOI: 10.1149/1.2967331.

[9] A. Hauch, S. Jensen, J. Bilde-Sorensen, and M. Mogensen. "Silica Segregation in the Ni/YSZ Electrode". In: *Journal of The Electrochemical Society* 154.7 (2007), A619. DOI: 10.1149/1.2733861.

[10] T. Matsui, R. Kishida, J.-Y. Kim, H. Muroyama, and K. Eguchi. "Performance Deterioration of Ni–YSZ Anode Induced by Electrochemically Generated Steam in Solid Oxide Fuel Cells". In: *Journal of The Electrochemical Society* 157.5 (2010), B776. DOI: 10.1149/1.3336830.

[11] M. A. Laguna-Bercero. "Recent advances in high temperature electrolysis using solid oxide fuel cells: A review". In: *Journal of Power Sources* 203 (Apr. 2012), pp. 4–16. DOI: 10.1016/j.jpowsour.2011.12.019.

[12] A. Hanifi, M. Laguna-Bercero, T. Etsell, and P. Sarkar. "The effect of electrode infiltration on the performance of tubular solid oxide fuel cells under electrolysis and fuel cell modes". In: *International Journal of Hydrogen Energy* 39.15 (May 2014), pp. 8002–8008. DOI: 10.1016/j.ijhydene.2014.03.071.

[13] P. Kim-Lohsoontorn, Y.-M. Kim, N. Laosiripojana, and J. Bae. "Gadolinium doped ceria-impregnated nickel-yttria stabilised zirconia cathode for solid oxide electrolysis cell". In: *International Journal of Hydrogen Energy* 36.16 (Aug. 2011), pp. 9420–9427. DOI: 10.1016/j.ijhydene.2011.04.199.

[14] Y. Chen, J. Bunch, C. Jin, C. Yang, and F. Chen. "Performance enhancement of Ni-YSZ electrode by impregnation of $Mo_{0.1}Ce_{0.9}O_{2+\delta}$". In: *Journal of Power Sources* 204 (Apr. 2012), pp. 40–45. DOI: 10.1016/j.jpowsour.2012.01.019.

[15] R. Xing, Y. Wang, S. Liu, and C. Jin. "Preparation and characterization of $(La_{0.75}Sr_{0.25})_{0.95}Cr_{0.5}Mn_{0.5}O_3$ - yttria stabilized zirconia cathode supported solid oxide electrolysis cells for hydrogen generation". In: *Journal of Power Sources* 208 (June 2012), pp. 276–281. DOI: 10.1016/j.jpowsour.2012.02.062.

[16] G. Tsekouras and J. T. S. Irvine. "The role of defect chemistry in strontium titanates utilised for high temperature steam electrolysis". In: *Journal of Materials Chemistry* 21.25 (2011), p. 9367. DOI: 10.1039/c1jm11313e.

[17] B. Ge, J. Ma, D. Ai, C. Deng, X. Lin, and J. Xu. "Sr_2FeNbO_6Applied in Solid Oxide Electrolysis Cell as the Hydrogen Electrode: Kinetic Studies by Comparison with Ni-YSZ". In: *Electrochimica Acta* 151 (Jan. 2015), pp. 437–446. DOI: 10.1016/j.electacta.2014.11.078.

[18] C. Bernuy-Lopez, R. Knibbe, Z. He, X. Mao, A. Hauch, and K. A. Nielsen. "Electrochemical characterisation of solid oxide cell electrodes for hydrogen production". In: *Journal of Power Sources* 196.9 (May 2011), pp. 4396–4403. DOI: 10.1016/j.jpowsour.2010.10.102.

[19] S. Xu, S. Chen, M. Li, K. Xie, Y. Wang, and Y. Wu. "Composite cathode based on Fe-loaded LSCM for steam electrolysis in an oxide-ion-conducting solid oxide electrolyser". In: *Journal of Power Sources* 239 (Oct. 2013), pp. 332–340. DOI: 10.1016/j.jpowsour.2013.03.182.

[20] Y. Gan, Q. Qin, S. Chen, Y. Wang, D. Dong, K. Xie, and Y. Wu. "Composite cathode $La_{0.4}Sr_{0.4}TiO_{3-\delta}$-$Ce_{0.8}Sm_{0.2}O_{2-\delta}$ impregnated with Ni for high-temperature steam electrolysis". In: *Journal of Power Sources* 245 (Jan. 2014), pp. 245–255. DOI: 10.1016/j.jpowsour.2013.06.107.

[21] M. Ni, M. Leung, and D. Leung. "Technological development of hydrogen production by solid oxide electrolyzer cell (SOEC)". In: *International Journal of Hydrogen Energy* 33.9 (May 2008), pp. 2337–2354. DOI: 10.1016/j.ijhydene.2008.02.048.

[22] M. Laguna-Bercero and V. Orera. "Micro-spectroscopic study of the degradation of scandia and ceria stabilized zirconia electrolytes in solid oxide electrolysis cells". In: *International Journal of Hydrogen Energy* 36.20 (Oct. 2011), pp. 13051–13058. DOI: 10.1016/j.ijhydene.2011.07.082.

[23] K. Eguchi. "Power generation and steam electrolysis characteristics of an electrochemical cell with a zirconia- or ceria-based electrolyte". In: *Solid State Ionics* 86-88 (July 1996), pp. 1245–1249. DOI: 10.1016/0167-2738(96)00295-0.

[24] A. Nechache, M. Cassir, and A. Ringuedé. "Solid oxide electrolysis cell analysis by means of electrochemical impedance spectroscopy: A review". In: *Journal of Power Sources* 258 (July 2014), pp. 164–181. DOI: 10.1016/j.jpowsour.2014.01.110.

[25] F. H. van Heuveln. "Electrode Properties of Sr-Doped $LaMnO_3$[sub 3] on Yttria-Stabilized Zirconia". In: *Journal of The Electrochemical Society* 144.1 (1997), p. 126. DOI: 10.1149/1.1837374.

[26] J. R. Mawdsley, J. D. Carter, A. J. Kropf, B. Yildiz, and V. A. Maroni. "Post-test evaluation of oxygen electrodes from solid oxide electrolysis stacks". In: *International Journal of Hydrogen Energy* 34.9 (May 2009), pp. 4198–4207. DOI: 10.1016/j.ijhydene.2008.07.061.

[27] A. Momma, T. Kato, Y. Kaga, and S. Nagata. "Polarization Behavior of High Temperature Solid Oxide Electrolysis Cells (SOEC)". In: *Journal of the Ceramic Society of Japan* 105.1221 (1997), pp. 369–373. DOI: 10.2109/jcersj.105.369.

[28] M. Keane, M. K. Mahapatra, A. Verma, and P. Singh. "LSM-YSZ interactions and anode delamination in solid oxide electrolysis cells". In: *International Journal of Hydrogen Energy* 37.22 (Nov. 2012), pp. 16776–16785. DOI: 10.1016/j.ijhydene.2012.08.104.

[29] K. Chen and S. P. Jiang. "Failure mechanism of (La,Sr)MnO_3 oxygen electrodes of solid oxide electrolysis cells". In: *International Journal of Hydrogen Energy* 36.17 (Aug. 2011), pp. 10541–10549. DOI: 10.1016/j.ijhydene.2011.05.103.

[30] S. P. Simner, J. F. Bonnett, N. L. Canfield, K. D. Meinhardt, V. L. Sprenkle, and J. W. Stevenson. "Optimized Lanthanum Ferrite-Based Cathodes for Anode-Supported SOFCs". In: *Electrochemical and Solid-State Letters* 5.7 (2002), A173. DOI: 10.1149/1.1483156.

[31] G. C. et al. "Copper doped lanthanum strontium ferrite for reduced temperature solid oxide fuel cells". In: *Solid State Ionics* 175.1-4 (Nov. 2004), pp. 73–78. DOI: 10.1016/j.ssi.2004.09.015.

[32] F. Tietz, V. Haanappel, A. Mai, J. Mertens, and D. Stöver. "Performance of LSCF cathodes in cell tests". In: *Journal of Power Sources* 156.1 (May 2006), pp. 20–22. DOI: 10.1016/j.jpowsour.2005.08.015.

[33] A. Endo. "Low Overvoltage Mechanism of High Ionic Conducting Cathode for Solid Oxide Fuel Cell". In: *Journal of The Electrochemical Society* 145.3 (1998), p. L35. DOI: 10.1149/1.1838332.

[34] V. M. Goldschmidt. "Die Gesetze der Krystallochemie". In: *Die Naturwissenschaften* 14.21 (May 1926), pp. 477–485. DOI: 10.1007/bf01507527.

[35] R. D. Shannon. "Revised effective ionic radii and systematic studies of interatomic distances in halides and chalcogenides". In: *Acta Crystallographica Section A* 32.5 (Sept. 1976), pp. 751–767. DOI: 10.1107/s0567739476001551.

[36] M. Senaris-Rodriguez and J. Goodenough. "$LaCoO_3$ Revisited". In: *Journal of Solid State Chemistry* 116.2 (May 1995), pp. 224–231. DOI: 10.1006/jssc.1995.1207.

[37] R. van Doorn. "Structural aspects of the ionic conductivity of $La_{1-x}Sr_xCoO_{3-\delta}$". In: *Solid State Ionics* 128.1-4 (Feb. 2000), pp. 65–78. DOI: 10.1016/s0167-2738(99)00282-9.

[38] J. Mastin, M.-A. Einarsrud, and T. Grande. "Structural and Thermal Properties of $La_{1-x}Sr_xCoO_{3-\delta}$". In: *Chemistry of Materials* 18.25 (Dec. 2006), pp. 6047–6053. DOI: 10.1021/cm061539k.

[39] F. Kröger and H. Vink. "Relations between the Concentrations of Imperfections in Crystalline Solids". In: *Solid State Physics*. Elsevier, 1956, pp. 307–435. DOI: 10.1016/s0081-1947(08)60135-6.

[40] G. Jonker and J. V. Santen. "Magnetic compounds with perovskite structure III. Ferromagnetic compounds of cobalt". In: *Physica* 19.1-12 (Jan. 1953), pp. 120–130. DOI: 10.1016/s0031-8914(53)80011-x.

[41] J. Mizusaki, Y. Mima, S. Yamauchi, K. Fueki, and H. Tagawa. "Nonstoichiometry of the perovskite-type oxides $La_{1-x}Sr_xCoO_{3-\delta}$". In: *Journal of Solid State Chemistry* 80.1 (May 1989), pp. 102–111. DOI: 10.1016/0022-4596(89)90036-4.

[42] S. Wang, M. Katsuki, M. Dokiya, and T. Hashimoto. "High temperature properties of $La_{0.6}Sr_{0.4}Co_{0.8}Fe_{0.2}O_{3-\delta}$ phase structure and electrical conductivity". In: *Solid State Ionics* 159.1-2 (Mar. 2003), pp. 71–78. DOI: 10.1016/s0167-2738(03)00027-4.

[43] A. Chainani, M. Mathew, and D. D. Sarma. "Electron-spectroscopy study of the semiconductor-metal transition in $La_{1-x}Sr_xCoO_3$". In: *Physical Review B* 46.16 (Oct. 1992), pp. 9976–9983. DOI: 10.1103/physrevb.46.9976.

[44] M. H. R. Lankhorst. "Determination of Oxygen Nonstoichiometry and Diffusivity in Mixed Conducting Oxides by Oxygen Coulometric Titration". In: *Journal of The Electrochemical Society* 144.4 (1997), p. 1268. DOI: 10.1149/1.1837581.

[45] M. H. R. Lankhorst, H. J. M. Bouwmeester, and H. Verweij. "Use of the Rigid Band Formalism to Interpret the Relationship between O Chemical Potential and Electron Concentration in $La_{1-x}Sr_xCoO_{3-\delta}$". In: *Physical Review Letters* 77.14 (Sept. 1996), pp. 2989–2992. DOI: 10.1103/physrevlett.77.2989.

[46] M. Sogaard, P. Hendriksen, M. Mogensen, F. Poulsen, and E. Skou. "Oxygen nonstoichiometry and transport properties of strontium substituted lanthanum cobaltite". In: *Solid State Ionics* 177.37-38 (Dec. 2006), pp. 3285–3296. DOI: 10.1016/j.ssi.2006.09.005.

[47] M. H. Lankhorst, H. Bouwmeester, and H. Verweij. "High-Temperature Coulometric Titration of $La_{1-x}Sr_xCoO_{3-\delta}$: Evidence for the Effect of Electronic Band Structure on Nonstoichiometry Behavior". In: *Journal of Solid State Chemistry* 133.2 (Nov. 1997), pp. 555–567. DOI: 10.1006/jssc.1997.7531.

[48] J. Jamnik and J. Maier. "Generalised equivalent circuits for mass and charge transport: chemical capacitance and its implications". In: *Physical Chemistry Chemical Physics* 3.9 (2001), pp. 1668–1678. DOI: 10.1039/b100180i.

[49] J. Fleig, A. Schmid, G. M. Rupp, C. Slouka, E. Navickas, L. Andrejs, H. Hutter, L. Volgger, and A. Nenning. "The Chemical Capacitance as a Fingerprint of Defect Chemistry in Mixed Conducting Oxides". In: *Acta Chimica Slovenica* (Sept. 2016), pp. 509–518. DOI: 10.17344/acsi.2016.2302.

[50] J. Jamnik. "Treatment of the Impedance of Mixed Conductors Equivalent Circuit Model and Explicit Approximate Solutions". In: *Journal of The Electrochemical Society* 146.11 (1999), p. 4183. DOI: 10.1149/1.1392611.

[51] A. K. Opitz and J. Fleig. "Investigation of O_2 reduction on Pt/YSZ by means of thin film microelectrodes: The geometry dependence of the electrode impedance". In: *Solid State Ionics* 181.15-16 (June 2010), pp. 684–693. DOI: 10.1016/j.ssi.2010.03.017.

[52] G. M. Rupp, H. Téllez, J. Druce, A. Limbeck, T. Ishihara, J. Kilner, and J. Fleig. "Surface chemistry of $La_{0.6}Sr_{0.4}CoO_{3-\delta}$ thin films and its impact on the oxygen surface exchange resistance". In: *Journal of Materials Chemistry A* 3.45 (2015), pp. 22759–22769. DOI: 10.1039/c5ta05279c.

[53] G. M. Rupp, A. Limbeck, M. Kubicek, A. Penn, M. Stöger-Pollach, G. Friedbacher, and J. Fleig. "Correlating surface cation composition and thin film microstructure with the electrochemical performance of lanthanum strontium cobaltite (LSC) electrodes". In: *J. Mater. Chem. A* 2.19 (2014), pp. 7099–7108. DOI: 10.1039/c3ta15327d.

[54] M. Kubicek, A. Limbeck, T. Frömling, H. Hutter, and J. Fleig. "Relationship between Cation Segregation and the Electrochemical Oxygen Reduction Kinetics of $La_{0.6}Sr_{0.4}CoO_{3-\delta}$ Thin Film Electrodes". In: *Journal of The Electrochemical Society* 158.6 (2011), B727. DOI: 10.1149/1.3581114.

[55] F. S. Baumann, J. Fleig, M. Konuma, U. Starke, H.-U. Habermeier, and J. Maier. "Strong Performance Improvement of $La_{0.6}Sr_{0.4}Co_{0.8}Fe_{0.2}O_{3-\delta}$ SOFC Cathodes by Electrochemical Activation". In: *Journal of The Electrochemical Society* 152.10 (2005), A2074. DOI: 10.1149/1.2034529.

[56] T. Kawada, J. Suzuki, M. Sase, A. Kaimai, K. Yashiro, Y. Nigara, J. Mizusaki, K. Kawamura, and H. Yugami. "Determination of Oxygen Vacancy Concentration in a Thin Film of $La_{0.6}Sr_{0.4}CoO_{3-\delta}$ by an Electrochemical Method". In: *Journal of The Electrochemical Society* 149.7 (2002), E252. DOI: 10.1149/1.1479728.

[57] F. S. Baumann, J. Fleig, H.-U. Habermaier, and J. Maier. "Impedance spectroscopic study on well-defined (La,Sr)(Co,Fe)$O_{3-\delta}$ model electrodes". In: *Solid State Ionics* 177.11-12 (Apr. 2006), pp. 1071–1081. DOI: 10.1016/j.ssi.2006.02.045.

[58] D. The, S. Grieshammer, M. Schroeder, M. Martin, M. A. Daroukh, F. Tietz, J. Schefold, and A. Brisse. "Microstructural comparison of solid oxide electrolyser cells operated for 6100 h and 9000 h". In: *Journal of Power Sources* 275 (Feb. 2015), pp. 901–911. DOI: 10.1016/j.jpowsour.2014.10.188.

[59] O. Yamamoto, Y. Takeda, R. Kanno, and M. Noda. "Perovskite-type oxides as oxygen electrodes for high temperature oxide fuel cells". In: *Solid State Ionics* 22.2-3 (Jan. 1987), pp. 241–246. DOI: 10.1016/0167-2738(87)90039-7.

[60] T. Huber, A. Opitz, M. Kubicek, H. Hutter, and J. Fleig. "Temperature gradients in microelectrode measurements: Relevance and solutions for studies of SOFC electrode materials". In: *Solid State Ionics* 268 (Dec. 2014), pp. 82–93. DOI: 10.1016/j.ssi.2014.10.002.

[61] E. McCalla, A. M. Abakumov, M. Saubanere, D. Foix, E. J. Berg, G. Rousse, M.-L. Doublet, D. Gonbeau, P. Novak, G. V. Tendeloo, R. Dominko, and J.-M. Tarascon. "Visualization of O-O peroxo-like dimers in high-capacity layered oxides for Li-ion batteries". In: *Science* 350.6267 (Dec. 2015), pp. 1516–1521. DOI: 10.1126/science.aac8260.